A hyperspectral and multi-angular synthetic dataset for algorithm development in waters of varying trophic levels and optical complexity

Jaime Pitarch[1], Vittorio Ernesto Brando[1,2]

[1]Consiglio Nazionale delle Ricerche (CNR), Istituto di Scienze Marine (ISMAR), Via Fosso del Cavaliere 100, 00133 Rome, Italy
[2]Commonwealth Scientific and Industrial Research Organisation (CSIRO), Environment, Canberra, Australia

Correspondence to: Jaime Pitarch (jaime.pitarch@cnr.it)

Abstract. This data paper outlines the development and the structure of a new synthetic dataset within an extended optical domain, encompassing inherent and apparent optical properties (IOPs-AOPs) alongside associated optically active constituents (OACs). Bio-optical modeling benefited from knowledge and data accumulated over the past three decades, enabling the imposition of rigorous quality standards and the definition of novel bio-optical relationships that are significant contributions on their own. Employing the Hydrolight scalar radiative transfer equation solver, above-surface and submarine light fields between 350 nm and 800 nm at 1 nm steps were generated, facilitating algorithm development and assessment for present and forthcoming hyperspectral satellite missions. A smaller version of the dataset, delivered at twelve Sentinel-3 OLCI bands (400 nm to 753 nm), was also produced, targeting multispectral sensor algorithm research. Derived AOPs encompass an array of above- and below-surface reflectances, diffuse attenuation coefficients, average cosines and the Q-factor. The dataset is distributed in 5000 files, each encapsulating a specific IOP scenario, ensuring sufficient data volume for each represented water type. AOPs are resolved across the complete range of solar and viewing zenith and azimuthal angles as per the Hydrolight default quadrants, amounting to 1300 angular combinations. This comprehensive directional coverage caters to studies investigating signal directionality, previously lacking sufficient reference data. The dataset is publicly available for anonymous retrieval via the FAIR repository Zenodo at https://doi.org/10.5281/zenodo.11637178 (Pitarch and Brando, 2024).

1. Introduction and review

1.1 Background

Marine optics studies the light that is measured by optical radiometers, whether in the water or above the surface. The optical signal is conveniently formulated in terms of apparent optical properties (AOPs), which are normalized quantities, less dependent on the intensity of the incident light than the radiances or irradiances from which they originate. The most notable AOP is the remote-sensing reflectance (R_{rs}), defined as the water-leaving radiance (L_w) per unit of above-water planar downwelling irradiance (E_s), and retrievable from satellite observations after atmospheric correction. Other quantities like diffuse attenuation coefficients, average cosines and the Q-factor find applications in marine optics too (Mobley, 1994).

AOPs are linked to the optically active water constituents (OACs), commonly phytoplankton and other suspended and dissolved substances. Phytoplankton is typically quantified in terms of the chlorophyll concentration (C) and non-living solids suspended in the water can be grouped in the non-algal particles (NAP), quantified by their concentration (N), though different splits of the particulate material are possible, such as particles of organic and inorganic origin, for example. Dissolved substances, optically categorized as colored dissolved organic matter (CDOM), are not commonly given in terms of mass concentration units, but in terms of the absorption coefficient spectrum, commonly at 440 nm (Y, or $a_g(440)$).

Empirical algorithms can be developed to invert any of the OACs from measured AOPs by finding statistical relationships between matched AOP and OAC data (IOCCG, 2006). This approach, although sometimes operationally robust and mechanistically meaningful, hampers progress in understanding the optical influence of OACs, which is given by the inherent optical properties (IOPs), namely the absorption and scattering coefficients. The IOPs can be mathematically linked to the OACs with the so-called bio-optical relationships, and to the AOPs through the radiative transfer equation, hence being a mathematical bridge between the AOPs and the OACs (Mobley, 1994).

The OACs are the independent variables that drive the generation of a synthetic dataset (SD). They can be a single quantity like C (IOCCG, 2006;Loisel et al., 2023), typically chosen for open sea conditions, or a triplet formed by C, N and Y (Nechad et al., 2015) or other combination, usually the choice for

optically complex waters. More variables give more flexibility but bio-optical relationships must be established for all of them to derive the IOPs. Statistical relationships between C and IOPs have been studied for decades (Bricaud et al., 1998;Loisel and Morel, 1998;Morel and Maritorena, 2001). Much less is known about N and Y, and in particular, in optically complex waters, where their bio-optical properties are much more regionally variable. Nevertheless, in the last two decades, fractional information on Australian waters (Blondeau-Patissier et al., 2009;Cherukuru et al., 2016;Blondeau-Patissier et al., 2017), European waters (Tilstone et al., 2012;Martinez-Vicente et al., 2010;Astoreca et al., 2012), South-African lakes (Matthews and Bernard, 2013) and North-American coastal waters (Aurin et al., 2010;Le et al., 2013;Le et al., 2015), and other localized areas, have contributed to a significant increase in the understanding of the bio-optics in optically complex waters.

Assuming an unpolarized submarine light field, IOPs consist of the wavelength (λ)-dependent absorption coefficient (a) and the volume scattering function (VSF; symbol β), which can be broken down to the contribution of the single OACs. For the setup used in this SD, consisting of phytoplankton, NAP and dissolved matter, the IOPs break down as in eq. (1**Error! Reference source not found.**), which includes the contribution by seawater itself and assumes that dissolved material does not significantly scatter light in the optical domain:

$$\begin{cases} a(\lambda) = a_w(\lambda) + a_{ph}(\lambda) + a_{NAP}(\lambda) + a_g(\lambda) \\ \beta(\Psi,\lambda) = \beta_w(\Psi,\lambda) + \beta_{ph}(\Psi,\lambda) + \beta_{NAP}(\Psi,\lambda) \end{cases} \quad (1)$$

For radiative transfer purposes, it is the total absorption coefficient a the relevant quantity. Instead, the VSF is resolved as a function of the scattering angle (Ψ). This creates a varying balance of the single contributors to scattering as their respective variabilities with Ψ are different. Specifically, the strongest differences are between water and the other particulate materials.

Because of the technical difficulties in measuring angularly-resolved scattering, most optical theory deals with angular integrals of the VSF, that are much more commonly measured with commercial instrumentation. If the VSF is integrated across the backward hemisphere, one obtains the backscattering coefficient (b_b), whereas if one integrates across all directions, one obtains the scattering coefficient (b). The total light attenuation along a direction is quantified with the beam attenuation coefficient ($c = a + b$). c is arguably the most measured IOP in all optics history and its bio-optics has been studied for many

decades, as opposed to b and especially b_b, whose measurements are much scarcer and more recent. c keeps the same additive property for each constituent, hence eq. (2):

$$\begin{cases} b_b(\lambda) = b_{bw}(\lambda) + b_{b,ph}(\lambda) + b_{b,NAP}(\lambda) \\ b(\lambda) = b_w(\lambda) + b_{ph}(\lambda) + b_{NAP}(\lambda) \quad (2) \\ c(\lambda) = c_w(\lambda) + c_{ph}(\lambda) + c_{NAP}(\lambda) + a_g(\lambda) \end{cases}$$

85 Given a certain constituent, whether phytoplankton or NAP, its VSF is normalized by its scattering coefficient to obtain the phase function (PF) as in eq. (3):

$$\tilde{\beta}_x = \frac{\beta_x}{b_x}, x = ph \text{ or } NAP \text{ (3)}$$

This normalization removes the variation of scale due to particle concentration so that the PF is a specific characteristic of the given particle type. For radiative transfer calculations, the PF must be set a priori for

90 each OAC. That can be a measured phase function (He et al., 2017), but more commonly from a family of simulated functions after electromagnetic scattering calculations (Morel et al., 2002;Fournier and Forand, 1994). In particular for the later case, Mobley et al. (2002) arranged an mathematical equation to select one PF from the Fournier-Forand PF family given the backscattering ratio, defined as in eq. (4):

$$B_x = \frac{b_{b,x}}{b_x}, x = ph \text{ or } NAP \text{ (4)}$$

95 Despite the fact that the bio-optical modelling for this SD considers the separate phytoplanktonic and non-algal parts individually, their scattering and attenuation coefficients cannot be measured separately Instead, there is literature on bio-optical relationships involving their "particle" aggregates as in eq. (5**Error! Reference source not found.**):

$$\begin{cases} b_{bp}(\lambda) = b_{b,ph}(\lambda) + b_{b,NAP}(\lambda) \\ b_p(\lambda) = b_{ph}(\lambda) + b_{NAP}(\lambda) \quad (5) \\ c_p(\lambda) = c_{ph}(\lambda) + c_{NAP}(\lambda) \end{cases}$$

100 Bulk absorption and attenuation are also commonly measured, that, after removing the water baselines, become the "non-water" components, as in eq. (6):

$$\begin{cases} a_{nw}(\lambda) = a_{ph}(\lambda) + a_{NAP}(\lambda) + a_g(\lambda) \\ c_{nw}(\lambda) = c_{ph}(\lambda) + c_{NAP}(\lambda) + c_g(\lambda) \end{cases} (6)$$

In order to develop updated bio-optical relationships and remote sensing algorithms, there is a need for large concomitant OAC-IOP-AOP datasets across a range of data values, seasons and geographical

locations, with fully characterized uncertainties. However, despite broader accessibility to field- and laboratory-based IOP instrumentation, current data availability and quality are below what was expected twenty-five years ago, when instrumentation became commercially available. Open access OAC-IOP-AOP datasets are scarce, strongly concentrated in some areas and without characterized uncertainties. Given this absence of data, it has been a common choice to develop SDs for optical studies (IOCCG, 2006;Nechad et al., 2015;Loisel et al., 2023). Their IOP-AOP relationships can be considered error-free, as they are derived from the solution of the radiative transfer equation, yet this exact relationship does not confer validity to the SD *per se*, as the IOPs resulting from bio-optical modelling could be unrealistic. SDs have a history of applications to the development of algorithms of varying complexity, from semianalytical algorithms (Lee et al., 2002) to complex neural networks (Doerffer and Schiller, 2007). If different sun-view geometries are considered for the output AOPs given an IOP setup, the directional aspects of AOPs such as the diffuse attenuation coefficient (Lee et al., 2013) or the reflectance (Morel and Gentili, 1993, 1996;Morel et al., 2002;Park and Ruddick, 2005;Lee et al., 2011) can be studied and analytical models for these variations can be proposed.

New and forthcoming hyperspectral satellite ocean color sensors, such as NASA's PACE or ESA's CHIME are fostering research on inherently hyperspectral algorithms, that may potentially retrieve more information from the oceans than classical multispectral sensors. It is then timely to produce a hyperspectral SD that covers relevant spectral ranges of the aforementioned sensors, for a globally representative range of water types.

In the absence of hyperspectral ocean color data, hyperspectral SDs can help to understand how much information is embedded in some key bands of multispectral sensors. In this respect, Talone et al. (2024) used a preliminary version of this SD to propose a hyperspectral R_{rs} reconstruction scheme from AERONET-OC data, in order to validate satellite derived hyperspectral radiometric products, confirming the validity of the reconstruction in large portions of the visible spectrum with constrained uncertainties.

1.2 Existing synthetic datasets

Numerical models for computing light fields have been used for decades (Mobley et al., 1993). Some authors developed internal codes (D'Alimonte et al., 2010) while others released them to the public

(Chami et al., 2015;Rozanov et al., 2014). By far, the most popular code in the marine optics community has been Hydrolight (formerly from Sequoia Scientific, Inc., now from Numerical Optics, Ltd.), which is available upon purchase. Its popularity arises from, on one hand, the convenient data input management, which allows the simulation of every possible case study in ocean optics with relative ease, and the data output, which includes the full array of radiometric quantities and AOPs needed. Its prevalence in the field is such that all SDs reviewed in this paper, as well as the one presented here, were generated with Hydrolight. It is therefore of importance that support and further development of Hydrolight is ensured for the future. This article only considers SDs that were publicly released. Only their main characteristics will be mentioned, especially those relevant to the new SD that we are presenting.

1.2.1 The IOCCG dataset

The first and the most cited of the SDs in this small review is the IOCCG SD (IOCCG, 2006). The release of this SD came at a time where the study of bio-optical relationships and the development of algorithms was at its all-time high (e.g., Twardowski et al., 2001;Loisel and Morel, 1998;Morel and Maritorena, 2001;Lee et al., 2002). It is a SD for testing and development of in-water algorithms in open and oceanic waters.

The single independent variable that drives IOP variability is the chlorophyll concentration (C), ranging from 0.03 to 30 mg m^{-3}. Phytoplankton absorption bio-optical modelling uses a database of a_{ph} spectra measured in the field. Given a C value, a random a_{ph} is chosen within the database, scaled by a factor, so that the scaled $a_{ph}(440)$ verifies an average relationship of the latter to C given by Bricaud et al. (1995), given by $a_{ph}(440) = A(440)C^{E(440)}$. Notably, the chosen a_{ph} belongs to a subset of a_{ph} spectra associated to C values within a narrow range of the given C. This choice implies assuming that a_{ph} spectra that are related to very different concentrations are not only different in magnitude, but also in shape.

The rest of bio-optical relationships are set after (mostly) published relationships, with the addition of some randomness that models the spread around the mean relationship, attributed to natural causes, and not captured by these average equations. While that choice is a positive feature of the SD, many parameterizations appear arbitrary.

The VSF is modelled after splitting the particulate matter in phytoplankton and NAP. The former scatters light following a Fournier-Forand phase function of fixed $B_{ph} = 0.01$, whereas the latter scatters light according to the average Petzold phase function, $B_{NAP} = 0.0183$. This is identified as a major limitation, as there are a number of concerns on the Petzold phase function that will be detailed below.

Radiances are available from 400 nm to 800 nm every 10 nm for the nadir view direction, and for two sun zenith angles (0 and 30 °).

1.2.2 The CoastColour dataset

The CoastColour SD (Nechad et al., 2015) was generated in the framework of an ESA project, aimed at the evaluation of algorithms for coastal waters. The project included the compilation of large amounts of in situ data, but the patchiness in the geographical and data range distributions and the disparity of measurement techniques, without quantified uncertainties, made evident the need of a SD that focused in such areas and associated data ranges.

The SD is driven by three OACs: phytoplankton, "mineral particles" and CDOM. This, in principle, ignores the contribution of non-algal particles of biological origin, but in practice, their "mineral particles" compartment *de facto* stands for "non-algal particles". 5000 triplets of their respective concentrations (C,N,Y) were randomly generated. Although not documented in their paper, these three constituents show some degree of linear crossed correlation, a feature that is seen in in situ datasets when these variables span across a large range. This choice also mechanistically avoids the generation of many unrealistic R_{rs} spectra coming from unrealistic (C,N,Y) triplets.

Bio-optical modelling relationships are based on average parameters and regression equations from literature, without randomization strategies to mimic natural variability. For example, phytoplankton absorption is modelled by simply applying the average "A" and "E" power law coefficients by Bricaud et al. (1995) at 440 nm for a given C, which makes all 5000 modelled R_{rs} have the same average pigment features. Furthermore, spectral slopes as well as the specific absorption and scattering coefficients at reference bands are set constant. Overall, these bio-optical choices create an optical uniformity that results in fictitiously tight relationships between various IOPs or between IOPs and AOPs, as well as their ratios, potentially misleading users about the performance of any algorithm that is evaluated.

185   Following the IOCCG approach, angular scattering is modelled by assuming a Fournier-Forand phase function for phytoplankton and the average Petzold phase function for NAP, with fixed backscattering ratios for both.

The SD delivers the absorption coefficient divided in the total non-water component and the phytoplankton absorption. To separate CDOM and NAP absorption, the users need to generate CDOM

190   spectra from the reported value at a given wavelength and the CDOM spectral slope.

AOPs are given from 350 nm to 900 nm every 5 nm, for the sun zenith angles 0, 40º and 60º, and the single nadir-viewing angle for radiances.

1.2.3 Loisel's dataset

Loisel's SD (Loisel et al., 2023) is mainly characterized by its effort to compensate the disproportionate

195   in situ data density from coasts and shelfs with respect to the open oceans, which cover a much larger area. Such disproportion in other datasets may have a biasing effect when developing optical algorithms based on AOP vs. IOP relationships, especially when the underlying goal is to represent a broad range of IOPs encountered within the global ocean. In this regard, Loisel's SD benefits from satellite-retrieved IOPs over the global oceans organized in histograms, used as guides to "trim" the in situ data histograms,

200   so that the data distributions in the SD closely match the global ones.

Bio-optical modelling follows the IOCCG approach with modifications. IOP variability is driven by chlorophyll concentration only, and phytoplankton absorption is taken randomly from a pool of real spectra, and then scaled. The CDOM and NAP spectral slopes are given random values within wide uniform distributions. This choice is preferrable to fixed values, yet some level of constrain with available

205   in situ data pools appeared possible instead.

Angular scattering of phytoplankton is modelled with a fixed Fournier-Forand phase function of $B_{ph} = 0.01$. There is, however, evidence (Whitmire et al., 2010) that B_{ph} varies across an order of magnitude. In Hydrolight, B_{ph} is used to choose the phase function, which, for a given b_{ph}, implicitly determines $b_{b,ph}$ and therefore, the amplitude of the signal. This detail is important when one seeks to replicate

210   relationships of b_{bp} to other IOPs that are found in measured data. NAP scattering is modelled as a spectral power law. Its angular scattering incorporates one innovation respect to the previous SDs by

dropping the Petzold phase function and using instead a Fournier-Forand function of $B_{NAP} = 0.018$, with such B_{NAP} close to the average Petzold value, but with an angular variation that resembles measured VSFs much more closely (Sullivan and Twardowski, 2009).

215   Output AOPs are given between the range 350 nm – 750 nm in steps of 5 nm. Several versions of the SD are available for various combinations of inelastic scattering being or not considered. Notably, this SD provides the data output at several depths. Simulations are made for the sun zenith angles 0, 30º and 60º, and the single nadir-viewing angle for radiances. All data are compiled in a single netCDF file for each type of simulation.

220   **1.3 Creating a new dataset**

This brief review of existing SDs has identified limitations that can be summarized in:

    (1) Overly simplified bio-optical parameters: spectral slopes, specific absorption or scattering at a reference wavelength, are often set as static values, mostly coming from dataset averages, thereby masking the optical diversity inherent within them. In this new SD, we address this limitation by

225   considering the variability of each optical parameter across available datasets and exploring their predictability as a function of other parameters.

    (2) An absence of constraints between absorption and scattering of a given water OAC: it is evident that absorption and scattering of a given AOC must exhibit statistical correlations due to their association with the same type of particles, but it is the rule that both properties are modelled

230   independently, potentially resulting in absorption-scattering pairs that do not accurately reflect the characteristics of naturally occurring particles. In this SD, we address this issue by leveraging in-situ data to constrain the modeling of both phytoplankton and NAP. This approach ensures that the corresponding absorption-scattering pairs align with all experimental evidence in statistical terms.

235   (3) Extrapolation of bio-optical relationships: a published relationship between two quantities is applied to different ones. For example, the average relationship between chlorophyll and particle scattering by Loisel and Morel (1998) has been used to model phytoplankton scattering, which is only a fraction of the total scattering.

(4) Limited validation of bio-optical models: some statistical relationships are presented without evidence. In situ datasets offer an opportunity to assess historical bio-optical relationships while also fostering the development of new ones, and such potential has not been yet fully developed.

(5) Limited spectral coverage of the blue-UV: in view of present and future satellite missions, it is desirable to generate SDs that at least cover the range from 350 nm.

(6) Limited directional AOP output: published SDs focus on the nadir viewing direction, for a few sun zenith angles. However, the light field is inherently directional, and ignoring directionality introduces errors in remote sensing algorithms. In consonance with a renewed impetus of optical studies that address the problem of directionality, it is aimed at generating a fully directional SD, accounting for all possible sun and view geometries.

2. Spectral IOPs data mining and reduction

The generation of bio-optical relationships needs support by in situ data, and a high quality is required, to be confident enough that the relationships that are found within the data are neither biased nor spurious. It was nevertheless assumed that data providers, based on their experience, followed best practices as most of these data were collected in the framework of optical studies funded by space agencies. Still, data was selected based on the usage of appropriate instrumentation and processing, when such information was available. Furthermore, selection criteria was rather aggressive, based on shape and fitness indices, overall providing confidence on the final retained data.

2.1 Phytoplankton absorption

Phytoplankton absorption a_{ph} has a complex spectral shape, which determines the small scale spectral features of related AOPs. For this reason, it is important to select high-quality a_{ph} data, suitable as input for radiative transfer simulations. For this SD, it was required that a_{ph} was sampled close to the surface of the water column, as bio-optical relationships involving phytoplankton seem to vary depending on the vertical layer (Bricaud et al., 1995;Loisel and Morel, 1998). In terms of spectral range, a condition was

imposed that a_{ph} has to be given at at least the range from 350 nm to 800 nm, which was a quite limiting requirement for the lower limit, as in most cases, a_{ph} is provided down to 400 nm or 380 nm.

265 Data were searched from the database SeaBaSS, providing many spectra, though a significant amount of them with anomalous spectral patterns. A PANGAEA search delivered many excellent spectra instead, collected in seven Polastern cruises (Soppa et al., 2013a;Liu et al., 2019b, c;Bracher, 2019;Bracher et al., 2021k;Bracher et al., 2021f;Bracher and Taylor, 2021), one Sonne cruise (Bracher et al., 2021l) and one Heincke cruise (Bracher et al., 2021c). The PACE dataset (Casey et al., 2020) was also used, in particular

270 data from the PI Schaeffer and from the Biosope cruise. In this latter case, the spectral range requirement was relaxed, allowing a maximum wavelength coverage of 750 nm, in order to keep necessary low-end a_{ph} that represent the clearest waters. At the high end of the range, Dr. A. Castagna's dataset on Belgian coastal and inland waters (Castagna et al., 2022) was used. Their published a_{ph} was only available from 380 nm, so Dr. Castagna kindly reprocessed the a_{ph} spectra down to 350 nm especially for this

275 investigation, though expressing some methodological concerns about the data accuracy in the UV. Finally, a new CNR small dataset from a recent cruise was also included in the global dataset.

In terms of selection and processing, the residual NIR value, estimated as the average a_{ph} between 780 nm and 800 nm (between 740 nm and 750 nm for Biosope), was subtracted. Given the high amount of data in total, it was preferred to apply rather aggressive filter selection criteria. Spectra were smoothed

280 with an 11 nm rectangular moving window to eliminate random noise introduced by the spectro-photometers. A noise parameter was calculated as the standard deviation of the difference between the unfiltered and the filtered a_{ph}, divided by a guess of the chlorophyll concentration based on $a_{ph}(665)$ after Bricaud et al. (1995). Spectra were retained if this noise parameter was lower than 0.002, except for the Biosope dataset, where the threshold was relaxed and raised to 0.004. Additionally, the absolute value

285 of the second derivative with respect to the wavelength, $|a_{ph}''|$, was calculated as a measure of spectral noise and spectra with the 90th percentile of $|a_{ph}''|$ between 350 nm and 800 nm lower than 0.0032 were selected.

Further selection criteria were applied based on spectral shape. We defined the following indexes:

$$m_{UV} = \min\{a_{ph}(\lambda \in [350 \text{ nm}, 450 \text{ nm}])\}$$
$$M_{UV} = \max\{a_{ph}(\lambda \in [350 \text{ nm}, 450 \text{ nm}])\}$$
$$M_G = \max\{a_{ph}(\lambda \in [550 \text{ nm}, 560 \text{ nm}])\}$$

(7)

$$I_{CHL} = \max\{a_{ph}(\lambda \in [650 \text{ nm}, 700 \text{ nm}])\} - \min\{a_{ph}(\lambda \in [650 \text{ nm}, 700 \text{ nm}])\}$$

290 Therefore, the following selection thresholds were applied to the indexes in eq. (7), which were chosen based on experience so that clearly anomalous spectra would be discarded yet trying not to penalize natural variability. These were $m_{UV}/I_{CHL} > 0.1$, $M_{UV}/I_{CHL} < 6$ and $M_G/M_{CHL} < 2$. In particular, the thresholds involving the UV discarded many spectra that raised excessively in the UV, likely consequence of insufficient bleaching of the filtered sample, or that tended to zero or even negative values instead. At

295 the green range, it was assumed that the spectrum shall present a valley or at least a value that is not much larger than the chlorophyll peak.

Finally, some spectra exhibited secondary peaks very distant from 676 nm, which was likely a sign of spectral misalignment. Therefore, it was required that such peak was between 670 nm and 681 nm for inclusion.

300 All the filtering procedures led to the selection of 3025 high quality a_{ph} spectra, representing a very wide range of values and water types.

2.2 CDOM absorption

CDOM absorption at 440 nm ($a_g(440)$ or Y) is one of the three independent variables of the bio-optical modelling. Its value is therefore given. Still, such value needs to be propagated to the whole spectrum by

305 assuming a spectral variation, modelled here as the usual exponential shape. The value of the spectral slope S_g and its potential relation to $a_g(440)$ must be determined after bio-optical modelling from a pool of in situ CDOM absorption spectra. CDOM is stored by filtering seawater with 0.2 μm pore size filters and absorption is measured through light transmission, as the scattering of the sample can be considered negligible. The most common measurement instrument is a bench spectrophotometer, where water is

310 poured in a cuvette of a given path length, usually between 1 cm and 10 cm. In clear waters, because of the short path length that makes resulting data very noisy, a liquid waveguide capillary cell (LWCC) system like UltraPath[TM] (World Precision Instruments, Inc.) is preferred, as it has a much larger path

length, up to 2 m, therefore obtaining proper optical densities for a given sample, even in the clearest waters. In this article, only open access CDOM data measured with UltraPath were selected in open ocean waters, whereas in complex coastal and inland waters, cuvette-based measurements were accepted as well. Therefore, the pooled CDOM data consisted of the PACE datasets Schaeffer, Biosope and Mouw, Castagna's measurements, as well as a large PANGAEA dataset based on several Polarstern cruises (Bracher et al., 2021a;Bracher et al., 2021b;Bracher et al., 2021i;Bracher et al., 2021h) and some smaller campaigns in coastal areas (Juhls et al., 2019;Hölemann et al., 2020;Bracher et al., 2021g;Pykäri, 2022). In all cases, data had to be provided at the range from 350 nm to 750 nm and close to the surface.

CDOM spectra were fitted to a decreasing exponential function with a given offset, $\hat{a}_{g,mod} = a_g(\lambda_0)e^{-S_g(\lambda-\lambda_0)} + a_{g,off}$ using non-linear least squares, with a bi-square weighting function to minimize the effect of outliers. Notably, fits were made in linear scale, as making them in logarithmic scale would artificially raise the weight of spectral regions where CDOM is less relevant. An excellent fit between model and data was required ($r^2 > 0.995$), to exclude shapes that did not verify the exponential assumption. Finally, the offset was removed: $a_{g,mod} = \hat{a}_{g,mod} - a_{g,off}$. The result of this procedure was 1168 $(a_g(\lambda_0), S_g)$ pairs.

2.3 NAP absorption

As with CDOM, NAP absorption spectra (a_{NAP}) are not introduced directly in the radiative transfer simulations but modelled as exponential functions. Data selection again prioritized quality as the data quantity was sufficient to derive statistical relationships. A PANGAEA search delivered data from various Polarstern cruises (Gonçalves-Araujo et al., 2018;Liu et al., 2019a, d;Wiegmann et al., 2019;Bracher et al., 2021j;Bracher et al., 2021e, d;Bracher and Liu, 2021;Soppa et al., 2013a, b) and one Heincke cruise (Bracher et al., 2021d). From the PACE database, a_{NAP} from the cruise Biosope and the PIs Mouw and Schaeffer were included. Castagna's measurements were also included, as well as recent CNR data.

An exponential shape was fitted, $\hat{a}_{NAP,mod} = a_{NAP}(\lambda_0)e^{-S_{NAP}(\lambda-\lambda_0)} + a_{NAP,off}$ in linear scale, and the condition $r^2 \geq 0.995$ was imposed. The offset was removed thereafter, $a_{NAP,mod} = \hat{a}_{NAP,mod} - a_{NAP,off}$, still recognizing that at least a part of $a_{NAP,off}$ might be physically realistic and not due to residual scatter errors. In such a case, it would be needed to pursue bio-optical relationships between

340    $a_{NAP,off}$ and other variables. In the absence of sufficient knowledge, we adopted the classical approach of removing the offset, as previous SDs (IOCCG, 2006;Nechad et al., 2015;Loisel et al., 2023). The result of this procedure was 1349 $(a_{NAP}(\lambda_0), S_{NAP})$ pairs.

2.4 CSIRO's dataset

Data collected in Australian waters by CSIRO researchers (Blondeau-Patissier et al., 2009;Blondeau-
345   Patissier et al., 2017;Cherukuru et al., 2016;Oubelkheir et al., 2023;Brando et al., 2012) contains several IOPs such as $a_{ph}(440)$, $a_{NAP}(440)$, $a_g(440)$, $b_{bp}(555)$, and an estimate of its spectral slope (η). Also, the chlorophyll concentration (C) and the total suspended matter concentration (T) contained in the dataset.

3. Bio-optical modelling

350   The bio-optical modelling of the various terms of the absorption and scattering budgets as a function of the OACs will be explained with high detail in the following sub-sections. Readers interested in a comprehensive summary can find all sequential steps summarized in Table 1.

Table 1 Summary of the bio-optical modelling

$a_{ph}(\lambda)$	$a_{ph}(\lambda)$ from a quality-controlled database, adjusted by a factor to verify $a_{ph}(670) = A(670)C^{E(670)}$, $A(670) = 0.019093$, $E(670) = 0.95568$
$c_{ph}(\lambda)$ $\tilde{\beta}_{ph}(\Psi)$	$$c_{ph}(\lambda) = c_{ph}(660)\left(\frac{660}{\lambda}\right)^{n_1}$$ $$n_1 = -0.4 + \frac{1.6 + 1.2\mathfrak{R}}{1 + C^{0.5}}$$ $$\mathfrak{R} \leftarrow \mathcal{U}(0,1)$$ $$\tilde{\beta}_{ph}(\Psi) \sim FF(B_{ph})$$ $$B_{ph} \leftarrow \mathcal{N}(\mu, \sigma)$$ $$\mu = 0.002 + (0.01 - 0.002) \cdot \exp[-0.56\log_{10}(C)]$$ $$\sigma = 0.001(3 - \log_{10}(C)) + 0.001$$

$a_{NAP}(\lambda)$	$$a_{NAP}(\lambda) = N a_{NAP}^*(440) \cdot e^{-S_{NAP}(\lambda-440)}$$ $$\log_{10} a_{NAP}^*(440) \leftarrow \mathcal{N}(\mu, \sigma)$$ $$\mu = a\, e^{\left(b \log_{10}\frac{C}{N} + c\right)}$$ $$a = -0.1886, b = -1.055, c = -1.27$$ $$\sigma = 0.2627$$ S_{NAP} $$\leftarrow \begin{cases} \mathcal{U}(0.01, 0.035) \text{ if } a_{NAP}(440) < 4 \cdot 10^{-4} \text{ m}^{-1} \\ \text{Ln } \mathcal{N}(-0.308x - 5.101, -0.0558x + 0.1164) \text{ if } a_{NAP}(440) \in [4 \cdot 10^{-4}, 0.06) \text{ m}^{-1} \\ \mathcal{N}(0.011, 0.016) \text{ if } a_{NAP}(440) \geq 0.06 \text{ m}^{-1} \end{cases}$$
$c_{NAP}(\lambda),$ $\tilde{\beta}_{NAP}(\Psi)$	$$c_{NAP}(\lambda) = c_{NAP}(440)\left(\frac{\lambda}{440}\right)^{-\gamma_{NAP}}$$ $$\gamma_{NAP} \leftarrow \mathcal{N}(\mu, \sigma)$$ $$\mu = 0.7, \sigma = 0.3$$ $$c(440) = a_{NAP}(440) + b_{NAP}(440)$$ $$b_{NAP}(440) = \frac{b_{b,NAP}(440)}{B_{NAP}}$$ $$B_{NAP} \leftarrow \mathcal{U}(0.01, 0.02)$$ $$b_{b,NAP}(440) = Tb_{bp}(440) - b_{ph}(440)$$ $$T = N + 0.07C$$ $$b_{bp}^*(440) = b_{bp}^*(555)\left(\frac{440}{555}\right)^{-\eta}$$ $$\eta \leftarrow Burr(\alpha, c, k)$$ $$\alpha = 0.854, c = 4.586, k = 1.108$$ $$\log_{10} b_{bp}^*(555) \leftarrow \mathcal{N}(\mu, \sigma)$$ $$\mu = m \log_{10} a_{NAP}^*(440) + n$$ $$m = 0.6834, n = -0.9483$$ $$\sigma = 0.2627$$ $$\tilde{\beta}_{NAP}(\Psi) \sim FF(B_{NAP})$$

$a_g(\lambda)$	$$a_g(\lambda) = Ye^{-S_g(\lambda-440)}$$
S_g	$$\leftarrow \begin{cases} \mathcal{U}(0.01,0.025) \text{ if } a_g(440) < 0.02 \text{ m}^{-1} \\ \mathcal{N}(-0.00040161x + 0.017508, -0.0003012x + 0.001881) \text{ if } a_g(440) \in [0.02,5) \text{ m}^{-1} \\ \mathcal{U}(0.0143,0.017) \text{ if } a_g(440) \geq 5 \text{ m}^{-1} \end{cases}$$

3.1 Optically active constituents

It is intended to generate a SD that covers the widest possible range of optical water types. The historic case 1 assumption is inappropriate and an IOP definition based on a single index such as chlorophyll concentration (C) is therefore not adopted. Instead, a generic three-variables model is used, in which variability is driven by C, N and Y separately. However, C, N and Y shall not be completely independent because, if that were the case, the bio-optical modelling would generate unrealistic IOP combinations. Instead, C, N and Y may be expected to have a certain degree of general relationship, tighter for the smaller values, that are found in the ocean, and more scattered for the higher values.

Here, the partial relationship between the three variables in logarithmic scale was modelled with the generation of 5000 triplets, following three Burr type XII random probability density functions, $x \leftarrow \text{Burr}(\alpha, c, k)$, related by a cross correlation matrix among them with the off-diagonal elements $\rho_{CN} = 0.8$, $\rho_{CY} = 0.75$, $\rho_{YN} = 0.6$. Then, the derived random numbers were transformed to the actual (C,N,Y), variables with $X = 10^{x-d}$, where X is either C, N or Y, and x is their logarithmic counterparts. These parameters are summarized in Table 2. Because the Burr distribution does not have an upper bound, it generated very few outliers $C > 1000 \ mg \ m^{-3}, N > 2000 \ g \ m^{-3}$ and $Y > 100 \ m^{-1}$ (~0.2 % or less) that were considered excessive. Such realizations were re-generated with a log-normal distribution, with the mean and standard deviation calculated from the rest of the dataset.

Table 2 Parameters of the probabilistic modelling of the optically active constituents

	Burr distribution parameters	Scale coefficient

Variable	α	c	k	d
Chlorophyll concentration (C)	3	3	2	3
Non-algal particles concentration (N)	3	4	1	4
CDOM absorption coefficient at 440 nm (Y)	2	6	1.3	4
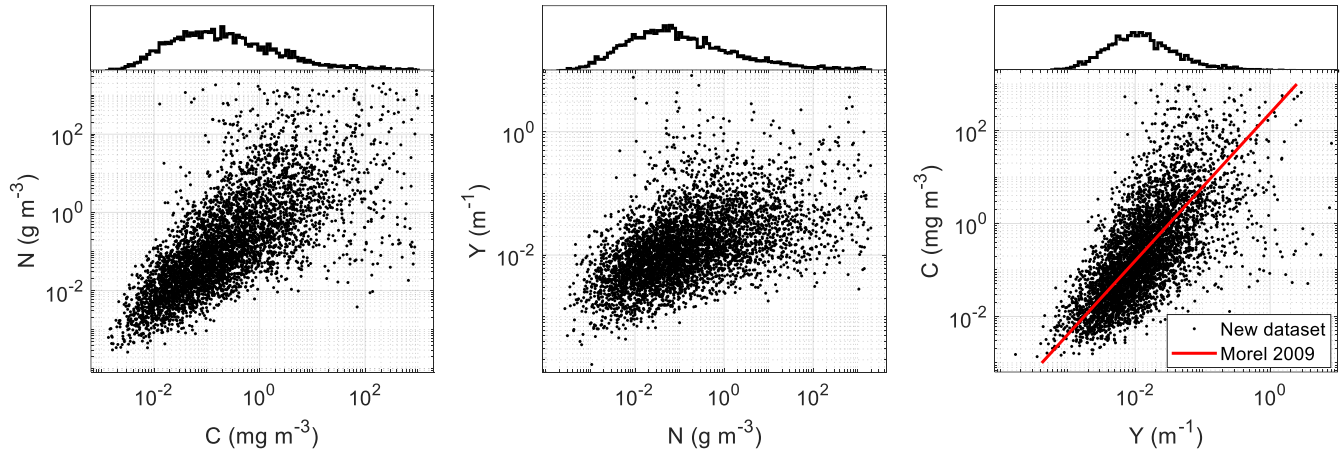
Figure 1: Upper panels: histograms of the water constituents chlorophyll concentration (C), non-algal particles concentration (N) and CDOM absorption at 440 nm (Y). Lower panels: relationships among them. For the relationship between C and Y, the average regression curve by Morel (2009) in oceanic waters is added for comparison.

In Fig. 1, the outcomes of OAC generation are depicted, showcasing broad ranges. The data distributions are skewed, mirroring histograms observed in broad range datasets: frequencies of data surge from the lower values, peak at levels commonly encountered in global oceans, and gradually taper off at higher extremes. Some degree of interrelationship is observable, which, in the case of C and Y, shows general agreement with the empirical case 1 curve by Morel (2009). As values ascend, the connection diminishes, consistent with expectations for coastal waters.

3.2 Phytoplankton absorption and scattering

Phytoplankton absorption a_{ph} was modelled using data from the pool described in section 2.1. In order to generate phytoplankton diversity, it was important to ensure that, each time, a real a_{ph} spectrum was used. A similar approach to the a_{ph} generation in the IOCCG SD was followed, but first, it was found

appropriate to revisit the relationship between C and a_{ph}. Matched data (Valente et al., 2022;Castagna et

390 al., 2022) at several wavelengths (Fig. 2) revealed a tight linear relationship in log-log scale, though with

some scatter, a part of which is attributable due to pigment variation. Following Bricaud et al. (1995), a

power-law model (eq. (8)) was regressed at each wavelength:

$$a_{ph}(\lambda) \approx A(\lambda) C^{E(\lambda)} \text{ (8)}$$

Table 3 Output variables and statistical metrics of the regression between matched chlorophyll
395 **concentration and phytoplankton absorption of the merged datasets Valente et al. (2022) and Castagna et**
al. (2022) at several bands.

λ (nm)	411	443	489	510	555	670
A	0.043934	0.051348	0.03299	0.02132	0.0077002	0.019093
E	0.80289	0.77654	0.76732	0.8214	0.92914	0.95568
n	3509	3526	3525	3507	3231	2875
RMSE (%)	58.951	59.249	57.358	52.626	56.781	47.256
r^2	0.85688	0.84553	0.84846	0.88033	0.89645	0.92553

Table 3 presents the regression outcomes, including the two model parameters (A,E), data number (n),

the root mean square in percent units and the coefficient of determination (r^2). A comparison to results

400 from previous publications (Churilova et al., 2023;Bricaud et al., 1995;Zibordi and Berthon, 2024) is

made in Fig. 3, showing some discrepancies respect to the first three references but a high agreement with

recent results by Zibordi and Berthon (2024).

Our results show that the 670 nm band has the highest capability for predicting C given a_{ph}. It is important

to emphasize that our modelling does not generate a_{ph} for a specific C; rather, it associates each a_{ph} with

405 its characteristic "C", from inversion of eq. (8). This enables to sort the 3025 a_{ph} spectra based on "C",

dividing them into 55 pools of specific "C" sub-ranges, each containing 55 spectra. Consequently, for a

given C value from the (C,N,Y) triplet, a random a_{ph} spectrum from the corresponding pool is selected.

Subsequently, the spectrum is adjusted by a factor so that $a_{ph}(670)$ equals the predicted $a_{ph}(670)$ from

C, after eq. (8). This methodology guarantees consistency between a_{ph} and empirical evidence for a given

410 C while ensuring a broad diversity in a_{ph} spectral shapes.
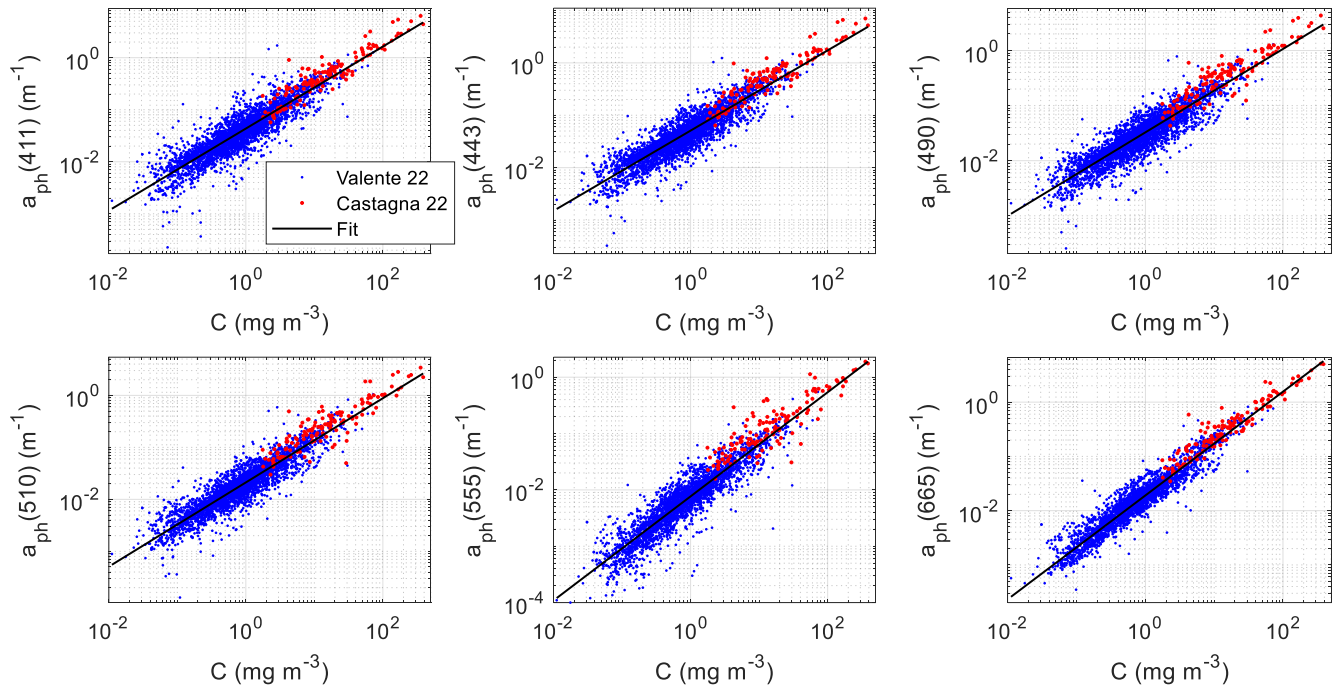
Figure 2: Matched C and a_{ph} data (Valente et al., 2022;Castagna et al., 2022) at six wavelengths. A linear fit in log-log form is displayed on top.
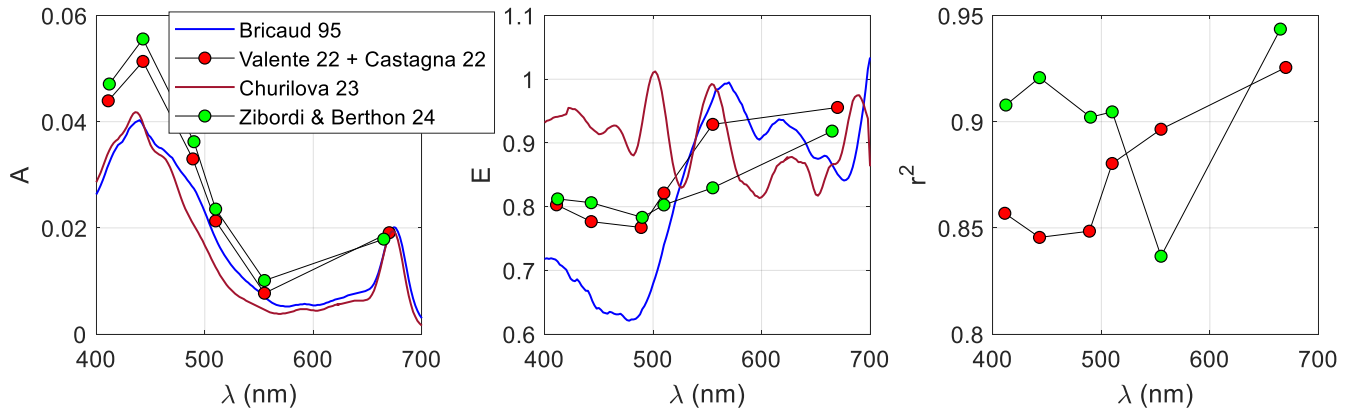
415

Figure 3: Regression statistics of the fit between C and a_{ph} data of Fig. 2. Left and center plots are Bricaud's A and E parameters, whereas the right plot is the coefficient of determination (r^2).

Phytoplankton scattering (b_{ph}) modelling unfortunately has much less background knowledge, mostly due to the lack of instruments that can measure in situ b_{ph} or $b_{b,ph}$. Electromagnetic modelling of light

420   scattering by particles suspended in water can be applied, although the contributions, albeit notable, are

limited (Lain et al., 2023;Poulin et al., 2018). Upon this lack, it is often referred to historic measurements by Loisel and Morel (1998) of non-water beam attenuation coefficient at 660 nm $c_{nw}(660)$ with a transmissometer, matched to chlorophyll concentration in case 1 waters. For surface waters, they found $c_{nw}(660) = 0.407C^{0.795}$. Furthermore, the authors reasonably assumed that the dissolved contribution

425   was secondary, so $c_p(660) \approx c_{nw}(660)$. Unfortunately, this relationship was directly exported to phytoplankton scattering modelling used in the CoastColour SD (Nechad et al., 2015), replacing $c_p(660)$ with $c_{ph}(660)$, ignoring that even in open sea waters, the non-algal scattering is considerable.

Here, the same generic power law dependence as in the IOCCG SD (IOCCG, 2006) is used:

$$c_{ph}(660) = p_3 C^h \text{ (9)}$$

430   According to the IOCCG report, $h = 0.57$, although application of eq. (9) to the downloadable SD reveals $h = 0.63$. In the CoasColour SD, $h = 0.795$. Here, $h = 0.7$ is used as a balance of both.

p_3 was set random between 0.06 and 0.6 in the IOCCG SD. Interestingly, that leaves the contribution of phytoplankton mostly below what found by Loisel and Morel (1998) for the total attenuation, which appears physically meaningful. The type of randomness of p_3 was not disclosed, but an inspection to the

435   IOCCG SD revealed that it was uniform. This parameter is modelled here like in the IOCCG SD given the absence of empirical evidence that justifies otherwise.

The spectral variation is set by assigning a power law to c_{ph}. A power law function provides a better fit for c_{ph} than for b_{ph}, as the latter is affected by anomalous dispersion effects, that result in some negative peaks with the shape of an a_{ph} spectrum, more evident at high phytoplankton concentrations (Bernard et

440   al., 2009). Interestingly, if the power law function is imposed to c_{ph}, the anomalous dispersion features b_{ph} automatically appear after $b_{ph} = c_{ph} - a_{ph}$. Therefore, in the current SD, neither b_{ph} nor $b_{b,ph}$ follow power law functions.

Regarding the actual exponent of the spectral power law, the same relationship as in the IOCCG SD is used, (eq. (10)):

445   $c_{ph}(\lambda) = c_{ph}(660) \left(\frac{660}{\lambda}\right)^{n_1}$, with $n_1 = -0.4 + \frac{1.6+1.2\Re}{1+C^{0.5}}$ (10)

With $\Re$ being a random number that follows a uniform distribution in the interval [0,1].

Given the randomness of a_{ph} and c_{ph}, it is possible that some realizations generate cases where $a_{ph} \geq c_{ph}$, which is unphysical. A given a_{ph} represents an assemblage of several phytoplankton communities, each with their specific scattering characteristics, that could be somewhat predicted given a_{ph}. This information could be extracted from the fine spectral features of a_{ph}. There are some simplified modelling results using electromagnetic theory for certain phytoplankton species (Lain et al., 2023), although a general modelling theory of phytoplankton scattering linked to absorption is still non-existent. Thus, in this SD, as in the precedent ones (IOCCG, 2006;Nechad et al., 2015;Loisel and Morel, 1998), a_{ph} and c_{ph} are modelled independently, yet related to the same chlorophyll concentration. To ensure a minimum degree of physical consistency, the procedure for determining a_{ph} and c_{ph} was repeated until ensuring $a_{ph} < c_{ph}$ at all wavelengths.

The remaining parameter to be set to run Hydrolight is the phytoplankton backscattering ratio, $B_{ph} = \frac{b_{b,ph}}{b_{ph}}$. This parameter has not been given much attention in previous research, as it was considered relatively unimportant, so it is common to find it set to a constant value in the order of 0.006 or 0.01. It is indeed secondary in semi-analytical algorithms that model R_{rs} from $\frac{b_b}{a+b_b}$ or variations, but in bio-optical modelling it can be very relevant if b_{ph} is fixed first, because then, $b_{b,ph}$ is implicitly determined through the choice of the respective phase function given B_{ph} (Mobley et al., 2002), thereby strongly influencing the intensity of R_{rs}. Fixing $b_{b,ph}$ first as a function of C would be another modelling option, for instance by adapting relationships between b_{bp} and C found in the ocean (Brewin et al., 2012) to $b_{b,ph}$.

In an effort to provide a more accurate determination of B_{ph} than in previous approaches, we propose a formula that is consistent with the general trend that phytoplankton size increases with C. In its turn, size increase lowers B_{ph} because larger particles scatter relatively more in the forward hemisphere respect to smaller ones, hence lowering B_{ph}. Twardowski et al. (2001; Fig. 11) presented pioneering results, for B_p in their case. Here, to mimic such effect, it is set

$$B_{ph} \sim \mathcal{N}(\mu, \sigma)$$

$$\mu = 0.002 + (0.01 - 0.002)\exp[-0.56\log_{10}(C)], \sigma = 0.001(3 - \log_{10}(C)) + 0.001 \quad (11)$$

To avoid unlikely low B_{ph} values after eq. (11), any realization delivering $B_{ph}<0.001$ was set to 0.001 as a lower limit.
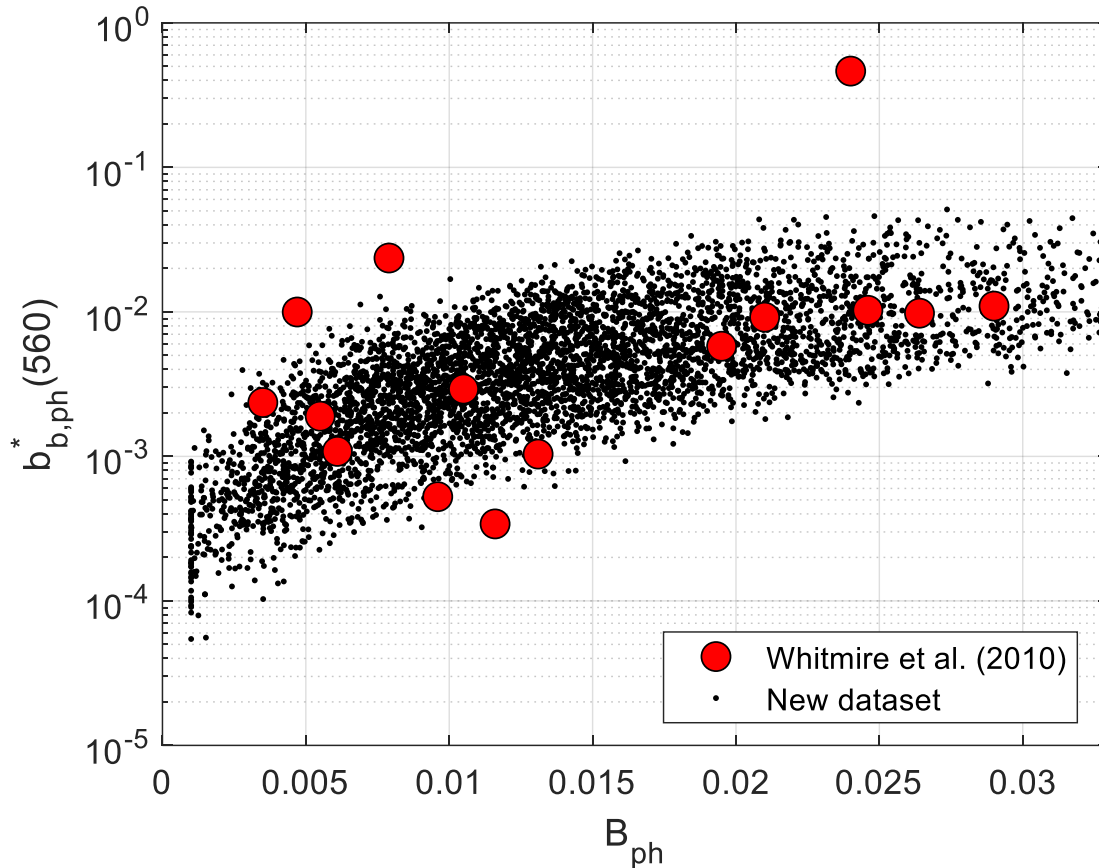
475

Figure 4: Phytoplankton backscattering ratio B_{ph} vs. phytoplankton specific backscattering coefficient at 560 nm $b_{b,ph}^*(560)$. Black dots: new SD. Red dots: data in Whitmire et al. (2010)

Independent validation of the modelling of phytoplankton scattering in eq. (11) is possible unique with data of chlorophyll concentration matched to scattering and backscattering for an array of phytoplankton

480 cultures by Whitmire et al. (2010). Calculating the chlorophyll-specific phytoplankton backscattering coefficient, i.e., $b_{b,ph}^* = \frac{b_{b,ph}}{C}$ at 560 nm, and matching it to B_{ph} produces dot clouds in Fig. 4. Our new SD follows the average trend displayed by the Whitmire et al. (2010) in situ data fairly well. Fig. 4 also shows some degree of positive covariation between $b_{b,ph}^*$ and B_{ph}. Indeed, $b_{b,ph}^*$ decreases with

increasing C as well because larger particles have a smaller surface area per unit volume, which diminishes specific scattering. A mechanistic model for b_{bp} that agrees with this principle was presented in Brewin et al. (2012). All in all, this leads to the visible correlation between B_{ph} and $b_{b,ph}^*$, with the scatter caused by species differences.

3.3 NAP absorption and scattering

Bio-optical modelling of NAP absorption a_{NAP} is complex, as NAP is formed by particles of very diverse nature, of biogenic and non-biogenic origin. Modelling approaches (Bengil et al., 2016) are valid as long as the derived relationships hold for the specific area of application. Here, it is aimed at a modelling approach of general validity, consistent with the in situ datasets that were collected from worldwide waters.

Modelling begins with linking a_{NAP} to the NAP concentration, N, through the specific absorption (to NAP concentration) a_{NAP}^*. Taking 440 nm as the reference band, other approaches have set it to a constant value (Nechad et al., 2015), although a variability between 0.001 and 0.1 m^2 g^{-1} was reported by Blondeau-Patissier et al. (2009) . When looking for a predictive formula, one may think that the actual value depends on the type of particles. Following this consideration the ratio C/N is proposed here as a first-order predictor of $a_{NAP}^*(440)$. This dependence assumes that NAP absorbs more efficiently in the relatively higher presence of chlorophyll, which suggests that NAP may be of biogenic origin to a larger extent than if the chlorophyll concentration was relatively lower, where NAP may be more of a mineral origin instead. CSIRO data confirmed some degree of covariation (Fig. 5). The fit to the CSIRO data was made in logarithmic scale, so $y = \log_{10}[a_{NAP}^*(440)]$ was regressed as a function of $x = \log_{10}\left(\frac{C}{N}\right)$, proposing a functional form of the type $y = a \exp(bx) + c$. A robust regression (bi-square weighting) gave $a = -0.1886, b = -1.0551, c = -1.2700$. The standard deviation of the fit was $\sigma = 0.2627$. To generate the synthetic data, given C/N, the regression curve was applied and then a random value, generated with a normal distribution $\mathcal{N}(0, \sigma)$ was added, in order to replicate the spread found in real data. $\frac{C}{N}$ in our SD covers a wider range than CSIRO's data, so, to avoid producing resulting synthetic

$a_{NAP}^*(440)$ values much out of the range of the measured data, the lower and upper bounds of -3 and -

510 0.5 were set for $\log_{10}[a_{NAP}^*(440)]$. The results are shown in Fig. 5.
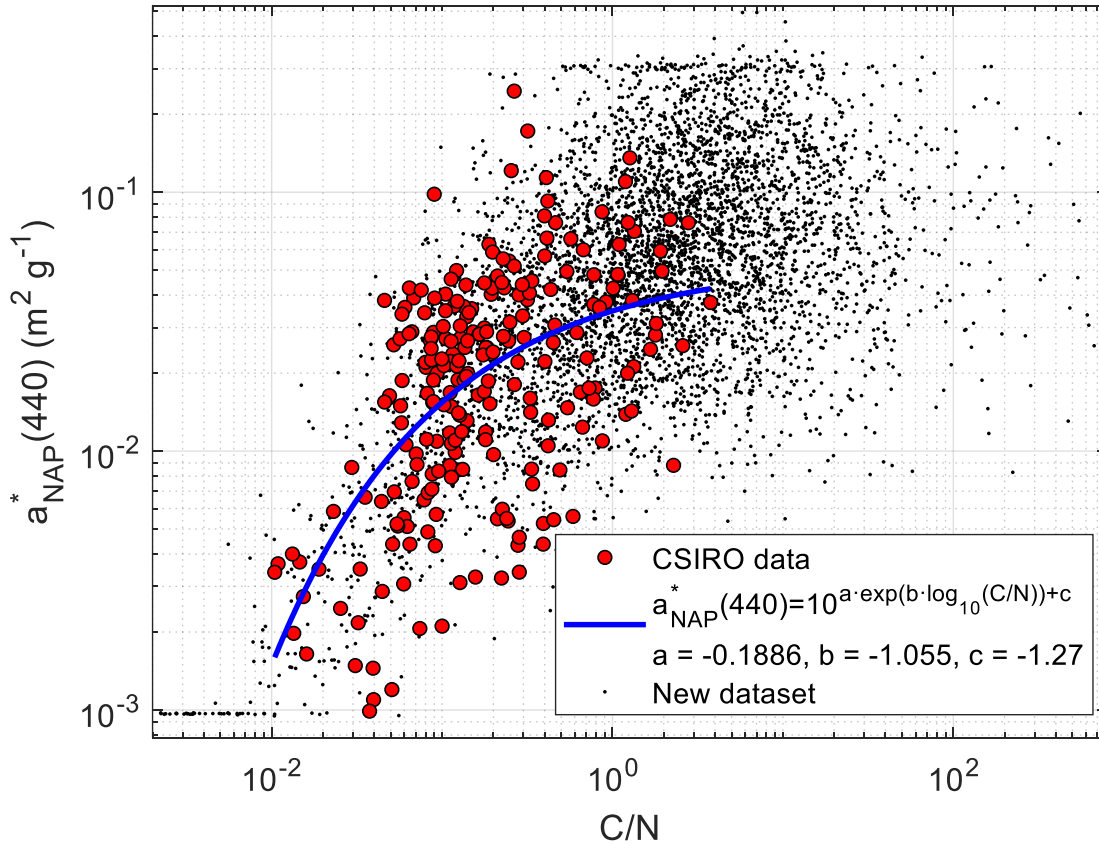
Figure 5: Non-algal particles specific absorption coefficient at 440 nm $a_{NAP}^*(440)$, plotted as a function of the chlorophyll to NAP concentrations ratio C/N. Results for CSIRO data in red dots, a best fit in blue, and generated data for the SD (black dots).

515 Posteriorly, it is necessary to project $a_{NAP}^*(440)$ to all bands. It can be done by assuming an exponential

spectral shape and then guessing a spectral slope (S_{NAP}). Historic data showed a distribution of S_{NAP} with

an average value of 0.0123 nm^{-1} (Babin et al., 2003), though with a significant spread. Using a single

average S_{NAP} for all simulations removes optical diversity and likely generates a_{NAP}^* spectra that are

unlikely for some regions. It is a better choice to generate a prediction function for S_{NAP} given the

520 available information. After the exponential fits for each of the compiled a_{NAP} spectra, detailed in section

2.3, the 1349 $(a_{NAP}(\lambda_0), S_{NAP})$ pairs were plotted together in Fig. 6.
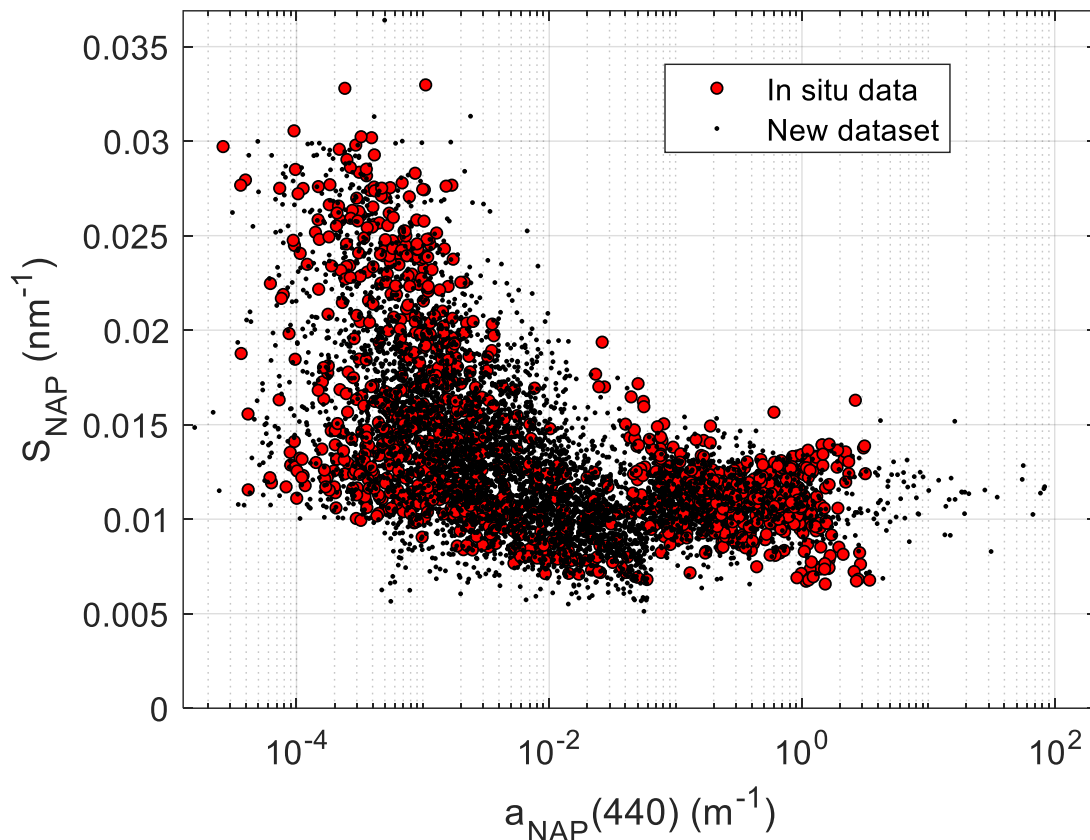
Figure 6: Non-algal particles absorption spectral slope (S_{NAP}), plotted as a function of the NAP absorption coefficient at 440 nm ($a_{NAP}(440)$). Red dots: in situ data. Black dots: synthetic data.

525   The data distribution in Fig. 6 shows a S_{NAP} spread that largely varies depending on the a_{NAP} range. For very small a_{NAP}, S_{NAP} shows no particular pattern between two bounds, so a uniform distribution was found adequate. For the middle range, the S_{NAP} distribution somewhat narrows as $a_{NAP}(440)$ increases, and data shows some positive skewness, which is well represented by a log-normal curve. For the higher $a_{NAP}(440)$ range, a gaussian distribution is apparent, in agreement with Babin et al. (2003). Therefore,

530   given $x = \log_{10}[a_{NAP}(440)]$, S_{NAP} was modelled as a piece-wise random distribution:

$$S_{NAP} \leftarrow \begin{cases} \mathcal{U}(0.01, 0.035) \text{ if } a_{NAP}(440) < 4 \cdot 10^{-4} \text{ m}^{-1} \\ Ln\,\mathcal{N}(-0.308x - 5.101, -0.0558x + 0.1164) \text{ if } a_{NAP}(440) \in [4 \cdot 10^{-4}, 0.06] \text{ m}^{-1} \\ \mathcal{N}(0.011, 0.016) \text{ if } a_{NAP}(440) \geq 0.06 \text{ m}^{-1} \end{cases} \quad (12)$$

Where $\mathcal{U}(a,b)$, $Ln\,\mathcal{N}(\mu,\sigma)$ and $\mathcal{N}(\mu,\sigma)$ are the uniform, log-normal and normal distributions, respectively. The random parameterization for S_{NAP} in eq. (12) is rather convoluted. However, it ensures

fitness to a high quality and large in situ dataset and it does not generate outliers, as it can be seen when overlapping the synthetic data to the field data in Fig. 6.

NAP scattering needs bio-optical modelling too. Approaches that model NAP absorption and scattering independently may generate unrealistic IOPs for that particular material. It is beneficial to look for relationships that link NAP scattering to NAP absorption, as it is expected to occur in natural waters. The CSIRO dataset contains $b_{bp}^*(555)$ data, concurrent to $a_{NAP}^*(440)$. It must be clarified that, while $a_{NAP}^*(440)$ is specific of N, b_{bp}^* has been defined by normalizing b_{bp} to the total suspended matter concentration (T), not to be confused with non-algal particles concentration N, as the latter is only a fraction of the former, which also contains the phytoplanktonic part. Brando and Dekker (2003) proposed a somewhat crude relationship, $T = N + 0.07C$, where both T and N are expressed in the usual units of g m^{-3} and C is in mg m^{-3}. For interested readers, such relationship was derived from measurements in a shallow, turbid and eutrophic lake in The Netherlands (Gons et al., 1992).
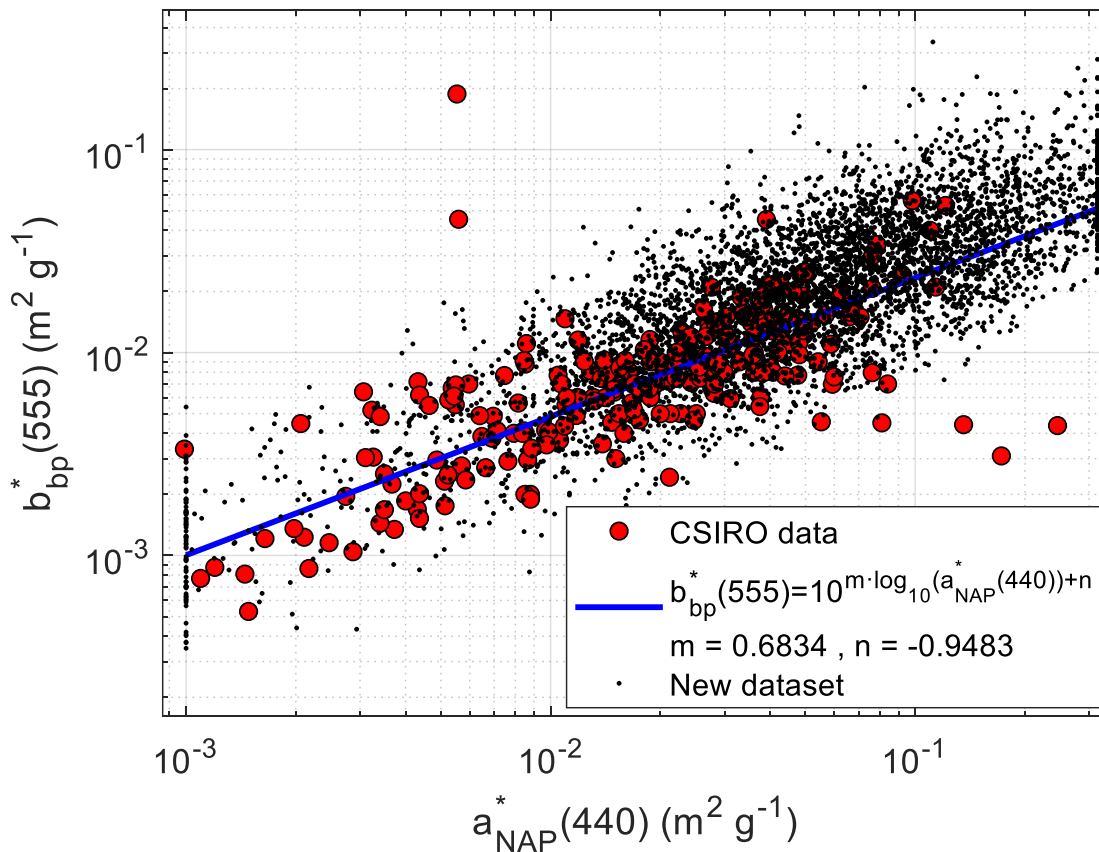
Figure 7: Specific particle backscattering coefficient at 555 nm $b_{bp}^*(555)$, plotted as a function of the non-algal particles specific absorption coefficient at 440 nm $a_{NAP}^*(440)$. Results for CSIRO data in red dots, the best linear fit in blue, and generated data for the SD (black dots).

550   The relationship between $a_{NAP}^*(440)$ and $b_{bp}^*(555)$ data is very marked (Fig. 7, red dots). A linear trend was a very good fit between the log-transformed variables, with a slope $m = 0.6834$ and an intercept $n = -0.9483$. The data spread followed a normal distribution ($\sigma = 0.2627$) after removing the trend line. To reproduce this spread in the SD, a random number following a random normal distribution $N(0, \sigma)$ was added to the fit-predicted $b_{bp}^*(555)$, prior to conversion to linear scale again. Results of the

555   data cloud generated are seen in Fig. 7, black dots.

Completing the bio-optical modelling for NAP requires to project b_{bp}^* from 555 nm to 440 nm. CSIRO data provides an estimate of the particle backscattering spectral slope (η) for every data point. For synthetic data generation, a modelling function for η must be derived. No relationship between η and any other parameter within the CSIRO dataset was found. Its histogram was fitted well with a random Burr

560   distribution with the parameters $\alpha = 0.854, c = 4.586, k = 1.108$, shown in Fig. 8 Therefore, η was randomly generated using this distribution.
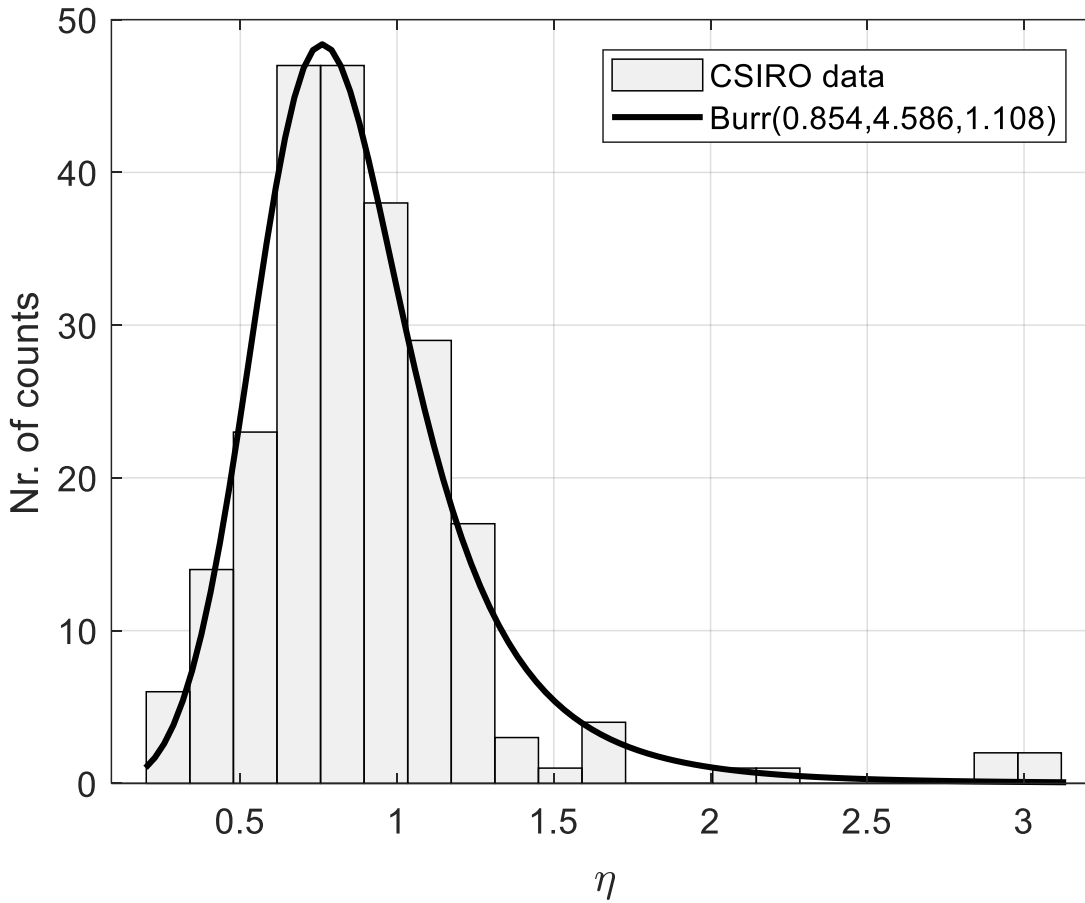
Figure 8: Histogram of the particle backscattering coefficient spectral slope (η). A Burr Type XII fitted distribution is plotted on top.

565

With η determined, b_{bp}^* was shifted to 440 nm: $b_{bp}^*(440) = b_{bp}^*(555) \left(\frac{440}{555}\right)^{-\eta}$. It must be remarked that this b_{bp} slope is only used in this step and it is not used to model b_{bp} with a power law in the SD. In the bio-optical modelling of NAP and of phytoplankton, a spectral shape is assumed for attenuation, not for backscattering.

570 The NAP backscattering at 440 nm was derived in eq. (13) by subtraction of the phytoplanktonic part, which is known from section 3.2:

$$b_{b,NAP}(440) = b_{bp}^*(440) \cdot T - b_{b,ph}(440) \text{ (13)}$$

A backscattering ratio for NAP (B_{NAP}) must be assumed to obtain $b_{NAP}(440)$ and $c_{NAP}(440)$. There are no direct measurements of B_{NAP} given the current impossibility of measuring NAP scattering parameters in the field. Nevertheless, this poses a minor problem for radiative transfer calculations, especially for remote sensing applications. As long as $b_{b,NAP}$ is fixed, B_{NAP} is relatively unimportant, as one can deduct from simplified analytical models for reflectance or diffuse attenuation. If b_{NAP} were fixed instead, B_{NAP} would be a fundamental parameter, as it would implicitly set $b_{b,NAP}$, in a much less accurate fashion. B_{NAP} was here fixed as a random number, following a uniform distribution between 0.01 and 0.02 as in eq. (15):

$$B_{NAP} \leftarrow \mathcal{U}(0.01, 0.02) \ (14)$$

Then, the scattering coefficient of NAP was determined with eq. (15):

$$b_{NAP}(440) = \frac{b_{b,NAP}(440)}{B_{NAP}} \ (15)$$

Then, the NAP attenuation at 440 nm was expressed in eq. (16) as a function of values that are all known:

$$c_{NAP}(440) = a^*_{NAP}(440) \cdot N + b_{NAP}(440) \ (16)$$

The remaining step for NAP modelling is extending NAP attenuation to all wavelengths. As for phytoplankton, a power law is assumed, and it is preferred to impose it to attenuation than to scattering, though recognizing that, given the much featureless shapes of NAP absorption, a fit to scattering may be realistic too. A c_{NAP} spectral slope γ_{NAP} must be assumed. This parameter is largely unknown as it cannot be measured in the field. Here, an educated guess is made, generating γ_{NAP} randomly, with $\gamma_{NAP} \leftarrow \mathcal{N}(0.7, 0.3)$. Therefore, eq. (17) completes the NAP modelling:

$$c_{NAP}(\lambda) = c_{NAP}(440) \left(\frac{440}{\lambda}\right)^{\gamma_{NAP}} \ (17)$$

3.4 CDOM absorption

The 1168 $(a_g(\lambda_0), S_g)$ pairs, calculated in section 2.2 are plotted together in Fig. 9. The middle section shows a data spread, whose mean and standard deviation decrease with $a_g(440)$. Variation in the lower and upper range ends could not be linked to any parameter, so that S_g was modelled as uniform distributions, fairly within the data range. Overall, S_g was then modelled as a piece-wise random distribution given $x = \log_{10}[a_g(440)]$:

$$S_g \leftarrow \begin{cases} \mathcal{U}(0.01, 0.025) \text{ if } a_g(440) < 0.02 \text{ m}^{-1} \\ \mathcal{N}(-0.00040161x + 0.017508, -0.0003012x + 0.001881) \text{ if } a_g(440) \in [0.02, 5) \text{ m}^{-1} \\ \mathcal{U}(0.0143, 0.017) \text{ if } a_g(440) \geq 5 \text{ m}^{-1} \end{cases} (18)$$

600
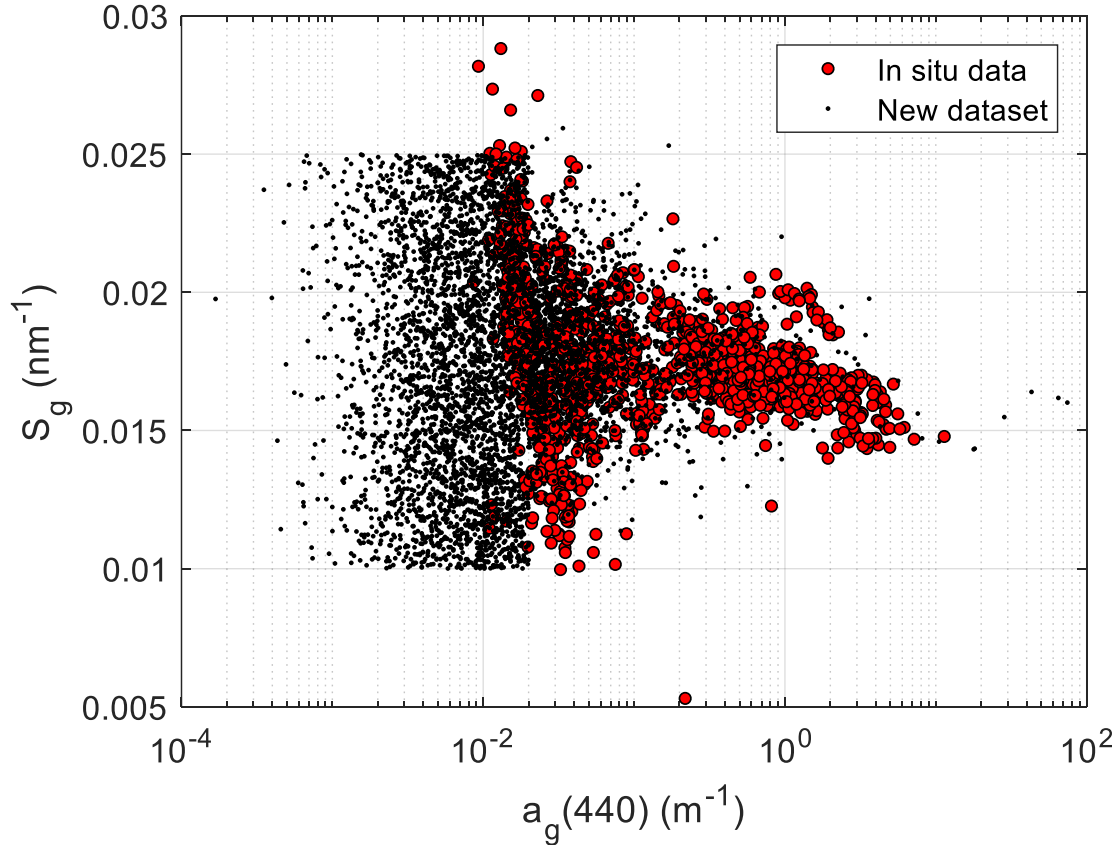
Figure 9: CDOM spectral slope (S_g), plotted as a function of the CDOM absorption coefficient at 440 nm ($a_g(440)$). Red dots: in situ data. Black dots: synthetic data.

605 Fig. 9 compares the field ($a_g(\lambda_0), S_g$) pairs to those generated with the combination of random distributions in eq. (18). It can be seen that the SD includes an order of magnitude more of $a_g(440)$ at the lower end than the in situ data in Fig. 9. This is due to the very stringent condition of exponential variation set in section 2.2, that mostly affected the low a_g spectra. In terms of predicting S_g, extrapolation may raise some concerns, but on one hand, S_g values are well bounded in this part of the

range, and on the other hand, one must also note that $a_g(440)$ becomes very low, so that potential errors in S_g are not relevant for the absorption budget. In terms of data range, it will be shown in section 4.1 that the lowest $a_g(440)$ in the SD are in the order of $a_g(440)$ in the most oligotrophic oceans.

3.5 Pure water absorption and scattering

Pure liquid water absorbs electromagnetic radiation, which can be mechanistically explained as the energy consumption by the two O-H molecular bonds to vibrate at given resonant frequencies, creating an absorption spectrum a_w with characteristic maxima and minima at specific wavelengths. In practice, a_w must be measured at a wide enough spectral range and its values be tabulated for usage in bio-optical modelling. However, literature only offers partial spectral range a_w measurements, owing to the specific requirements and challenges inherent in such measurements. A broad range a_w must then be a merged product from individual sources. A crucial step here involves compensating for the different temperatures at which a_w was measured in different laboratories and, in the spectral ranges where different measurements are available, selecting those that are retained of the highest quality. Fortunately, this process was already undertaken within the framework of an ESA project (Roettgers et al., 2016), where the "water optical properties processor" (WOPP) produced a dataset of pure water absorption, normalized to 20°C. Notably, this dataset encompasses measurements by Mason et al. (2016) from UV to green wavelengths, revealing lower water absorption in the UV and blue regions than previously documented, thanks to meticulous sample preparation and precise measurements. In other spectral regions, data from various authors are merged, sometimes overlapping spectrally and sometimes not. Overall, the WOPP pure water absorption data can be considered the state of the art. For comprehensive insights, readers are directed to the project report.

When marine salts are dissolved in water, the ions dissociate and create a stable solution whose absorption can be related to that of pure water proportionally to the salinity (Ψ_S), wavelength dependent. Temperature affects absorption in a similar manner through Ψ_T, thus leading to:

$$a_w(T, S) = a_w(T_0, 0) + \Psi_T(T - T_0) + \Psi_S S \quad (19)$$

635   Both Ψ_T and Ψ_S can be empirically determined. To the WOPP pure water merged absorption, a shift to an average ocean salinity of S=35 PSU was made with eq. (19), using the Ψ_S coefficient provided by Roettgers et al. (2014) for artificial seawater.

Scattering by pure water finds explanation with the Smoluchowski-Einstein fluctuation theory of light scattering (Zhang and Hu, 2021), according to which, a certain volume of water can be seen as made of
640   smaller sub-volumes that contain, on average, the same number of water molecules. However, the instantaneous numbers vary among them due to random thermal motions at the molecular level, resulting in microscopic density fluctuations that induce scattering. In the presence of solutes such as salts, this effect is magnified, as fluctuations in the spatial arrangement of dissolved ions lead to variations in the overall refractive index. For common ocean salinities, scattering is augmented by approximately 30%
645   respect to fresh water. Recent work by Zhang and Hu (2021) provides a comprehensive review of this theory, offering the most precise estimates to date (likely within ±2-4%). Nevertheless, rigorous experimental validation remains imperative. The formulas provided as supplementary material in their paper were employed to compute seawater scattering, assuming a temperature of T=20°C and a salinity of S=35 PSU, as for the absorption data.

650 **4. Results of the synthetic dataset**

4.1 Modelled IOPs

The bio-optical modelling detailed in the section 3 generated the IOPs that determine the resulting light field and related AOPs, given the boundary conditions. These bio-optical relationships have been individually assessed and consistency with literature and with new data has been ensured in that section.
655   However, the overall result of the bio-optical modelling can be tested by checking the crossed relationship between different commonly measured IOPs at specific wavelengths, compared to in situ data, in order to verify that the relationships that are found in the world's waters are represented.

In situ datasets were searched that contained IOP data at the reference wavelength of 440 nm. The following publicly available data were used: PACE data including the Biosope cruise data from the
660   clearest ultraoligotrophic waters of the south-Pacific gyre, plus some stations in coastal upwelling water

off Perú, and Mouw's data in Lake Superior (Casey et al., 2020), the NOMAD dataset (Werdell and Bailey, 2005), Castagna's data in Belgian coastal and inland waters (Castagna et al., 2022), measurements in coastal European waters (Massicotte et al., 2023), measurements in Svalbard (Petit et al., 2022) and a recently published dataset in European seas (Zibordi and Berthon, 2024). In addition, two datasets not yet publicly available were queried to the authors, who kindly sent them for use in this article: data from the Persian Gulf (Moradi and Arabi, 2023) and from Australian waters (Blondeau-Patissier et al., 2009;Blondeau-Patissier et al., 2017;Cherukuru et al., 2016;Oubelkheir et al., 2023;Brando et al., 2012). Castagna's data lacked b_{bp} but since such a dataset was considering unique and relevant, b_{bp} was inferred through semi-analytic closure from absorption and R_{rs} (Lee et al., 2011).
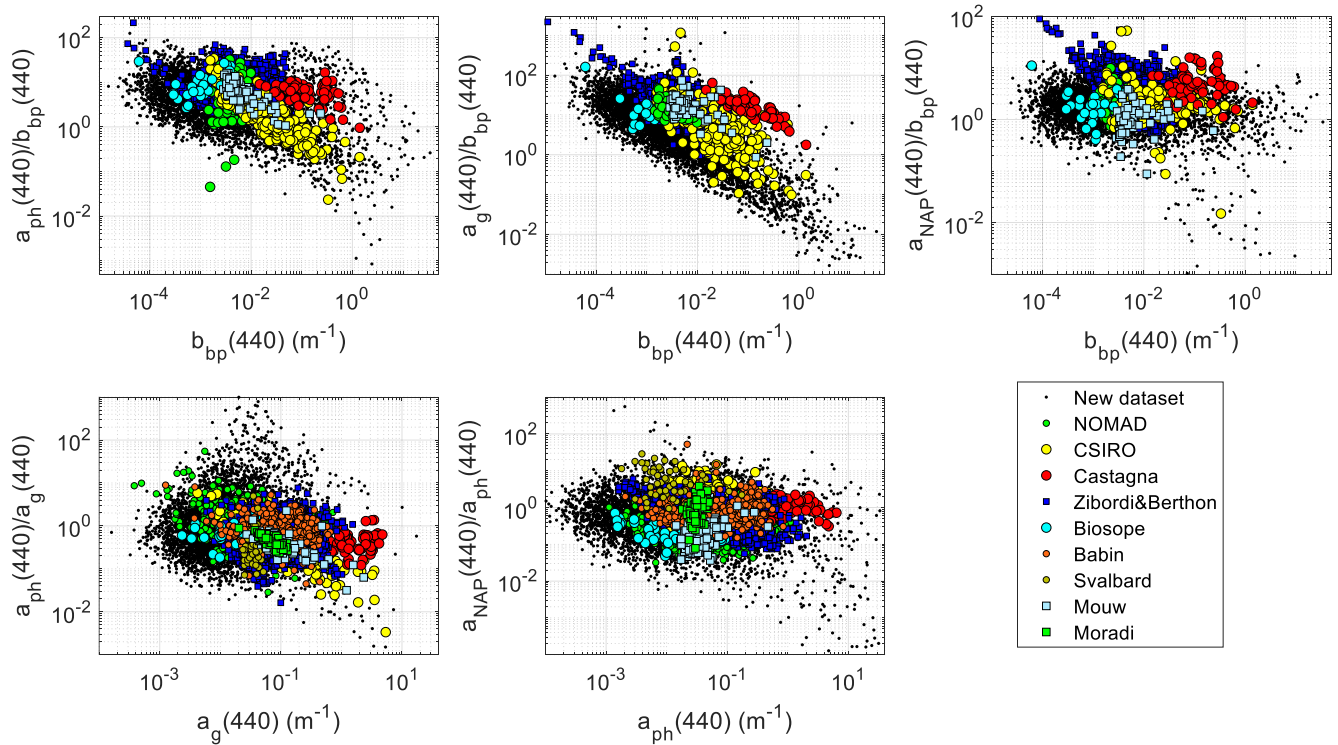
Figure 10: IOP cross-relationship comparison between the SD and various in situ datasets.

Fig. 10 presents relationships among various IOPs at the reference wavelength of 440 nm. The upper panels study the three non-water absorption components with respect to particle backscattering and the two lower panels compare the different absorption compartments. Because two given IOPs are expected

to linearly covary to the first degree, the vertical axis plots the ratio between the two, so that the linear covariation is eliminated, restricting the dynamic range and highlighting the differences among datasets. The plots show that available measurements in different geographic areas and seasons cover different regions of the data space, and that the SD globally encompasses all of them, notably extending the data volume in oligotrophic oceanic waters, that are geographically large but grossly under-sampled. Overall, this figure provides quite robust evidence that the SD has global coverage, from the clearest oceans to all kinds of coastal waters, and that the bio-optical relationships adopted in this study are in line with empirical evidence.
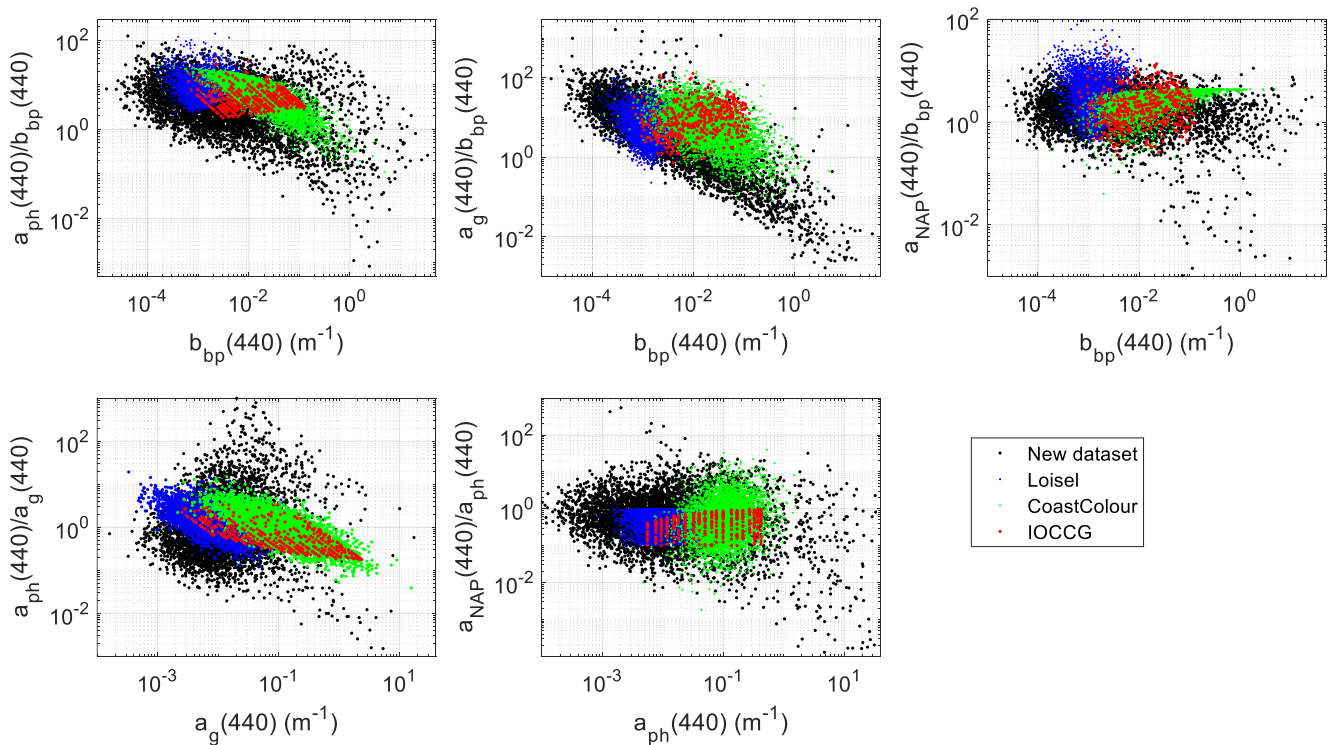
Figure 11: IOP cross-relationship comparison between this and other SDs.

This SD is also compared to the three publicly available SDs in Fig. 11: the IOCCG SD (IOCCG, 2006), the CoastColour SD (Nechad et al., 2015) and Loisel's SD (Loisel et al., 2023). Some overlap is noticeable for all crossed IOPs, with Loisel's SD more shifted towards clearer waters than IOCCG and CoastColour. Also, Loisel's SD shows trends that appear more consistent to our SD. The CoastColour SD covers the upper part of the range, but due to its optical modelling, many dots are clustered near each other, instead

of covering a wider range of values. The new SD covers a wider range of waters than the other SDs combined, a consequence not only of the broad ranges for the OACs, but also of the adequate amount of statistical randomness that was given to the bio-optical relationships.

4.2 Radiative transfer calculations

695 Radiative transfer simulations were made with Hydrolight 5.1.2 (Sequoia Scientific, Inc.). Normalized sky radiances were computed using the sky model "HCNRAD" (Harrison and Coombes Normalized RADiances) (Harrison and Coombes, 1988). Diffuse and direct sky irradiances were computed using the "RADTRANX" (RADTRAN eXtended for 300-1000 nm) model (Gregg and Carder, 1990). The ozone concentration was estimated from a climatology derived with binned monthly average TOMS v8 Ozone

700 concentrations (data from 2000-2004 were averaged to give 5-year climatological averages for 5° latitude and 10° longitude quadrants), for the 90th day of the year, coordinates 40 ° N and 0 ° E, resulting in 354.9 Dobson units. The US Navy aerosol model was fed with the values: air mass type 5, relative humidity 80.0 %, precipitable water 2.5 cm and horizontal visibility 40.0 km. Sea surface roughness was modelled with a Hydrolight-embedded Monte Carlo module, fed with an assumed wind speed of 5.0 m/s. Water

705 index of refraction was calculated as a function of wavelength (Roettgers et al., 2016) for the given seawater T = 20.0 ºC and S = 35.0 PSU. The sea was considered vertically homogeneous and infinitely deep. IOP input was configured with a generic "case 2" water scenario. Input IOP parameters and phase functions were set as detailed in Table 1. Inelastic scattering effects were not considered.

The source code of Hydrolight was modified so that the "printout" output files included reflectances, both

710 above and below the surface, for the whole set of viewing zenith and azimuth angles defined by Hydrolight default quadrants, that is, view angle varying from 0 to 80 ° in steps of 10 ° and then a last value of 87.5° (10 values in total), and azimuth varying from 0 to 180 ° in steps of 15 ° (13 values in total). Simulations were made for the whole range of sun zenith angles defined by the quadrants, that is from 0 to 80 ° in steps of 10 ° and then a last value of 87.5° (10 values in total). Therefore, for every IOP set up,

715 directional AOPs are given at 1300 angles, and non-directional AOPs are given at the 10 sun zenith angles.

4.3 Reflectance overview and classification

Synthetic R_{rs} were scrutinized to ensure that a diverse range of optical water types had been produced. The data underwent partitioning into twelve clusters via a k-means algorithm (Fig. 12). Ternary plots were employed to visualize the absorption budget for all R_{rs} within each class, with curves and dots colored based on particle backscattering. This classification is only used here as a method to show the extensive optical diversity within the SD and does not constitute a part of it. Descriptively, the following water types are:

- Classes 2 and 6 relate to clear oceanic waters.
- Class 1 corresponds to highly absorbing waters, with little NAP content.
- Classes 3,5, 7 and 8 represent coastal waters, exhibiting moderate concentrations of all constituents, in varying proportions.
- Classes 4 and 9 display highly productive waters, marked by high CDOM and NAP levels, respectively.
- Classes 10, 11 and 12 portray highly and very highly turbid waters. Notably, despite categorizing this water type into three classes, their cumulative occurrence is discrete. This outcome stems from the classification, which accentuates disparities in R_{rs} values that are high.
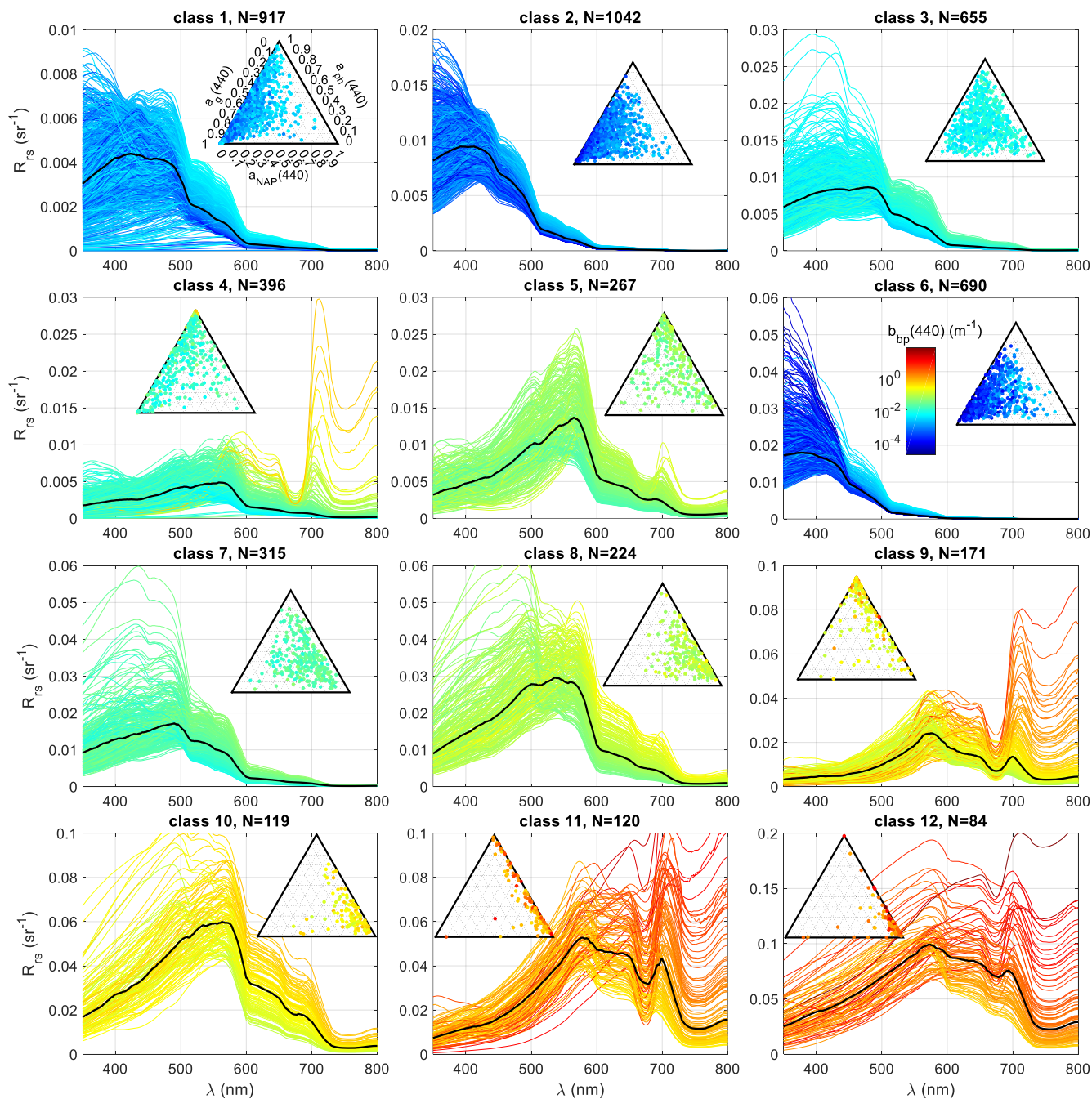
Figure 12 R_{rs} **spectra (normalized geometry) of the SD, divided into twelve classes using the k-means classifying algorithm, with their number (N) indicated above. Relative to each class, the ternary plots of the absorption budget are plotted. Line and dot color indicates particle backscattering at 440 nm, according to the attached color bar. Note varying vertical scale, across the classes, necessary to visualize the spectral variabilty across the dynamic ranges.**

4.4 Angular variation

740 Besides the wide IOP ranges, a unique characteristic of this SD is the resolution of the AOPs for the whole range of sun-view geometries. This matter is relevant for algorithm development and validation; for instance, in either in situ or satellite R_{rs}, the sun is very rarely at the zenith. The view angle is off nadir in above-water platforms and in satellite data, and the azimuth is normally such that avoids the maximum sun glint. This R_{rs} bidirectionality is very often ignored. Algorithms that use band ratios, such

745 as the oceanic OCx, partially suppress the bidirectional effect because its spectral pattern is quite flat, but algorithms that rely on the absolute magnitude of R_{rs} will inevitably propagate bidirectional effects as errors. This section showcases the anisotropy of R_{rs} for two distinct water types. The first represents very oligotrophic oceanic waters, while the second relates to more productive waters. The azimuthal angle definition follows that of Hydrolight (i.e., solar photons travel in the $\phi = 180°$ direction, that is, the sun

750 is located at $\phi = 0$).

A first example of the R_{rs} anisotropy for a clear water scenario is displayed in Fig. 13, for three wavelengths and five sun zenith angles. Related Fig. 14 focuses on one sun zenith angle ($\theta_s = 60°$), the sun's meridian plane ($\phi = 0, 180°$) and its perpendicular vertical plane ($\phi = -90, 90°$), and a constant zenith view section ($\theta = 60°$), all cases for a reference sun zenith angle ($\theta_s = 60°$). Increasing the sun

755 zenith lowers the azimuthal symmetry and strengthens the radiance anisotropy. A zone of higher values forms along the solar plane for $\phi = 0$. It is known that, for very clear waters, the single-scattering approximation can, at least qualitatively, explain the results. The phase functions of both water and particles have a local maximum at a scattering angle of $\Psi = 180°$, leading to an overall maximum at $\theta = 60°$, that is, the backscattering direction. The secondary maximum at $\theta = -60°$ (or $\theta = 60°$ for $\phi =$

760 $180°$) can be explained by the balance between a progressive increase in the particle phase function and a decrease in the water phase function as Ψ decreases.
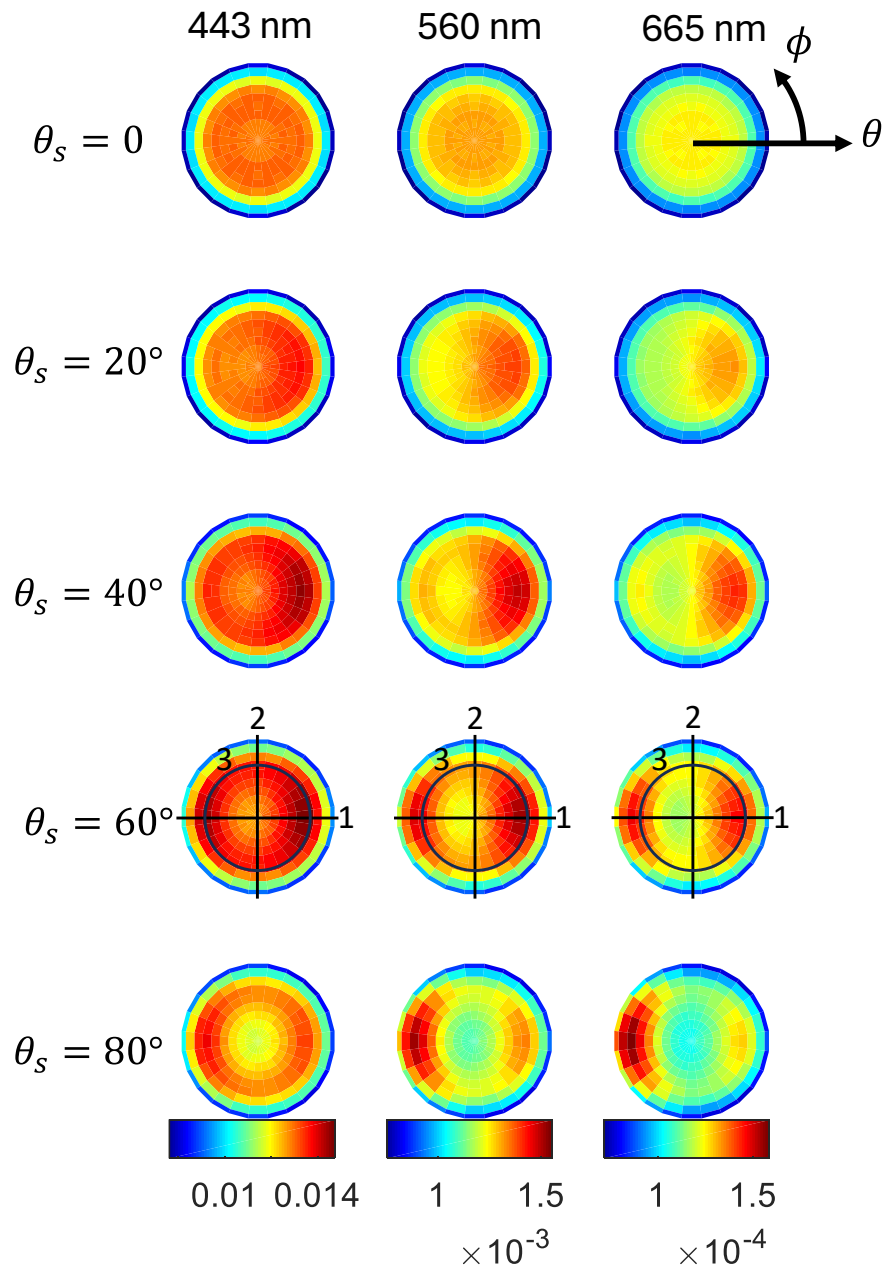
Figure 13 Angular variability of R_{rs} for the oligotrophic water spectrum shown in Fig. 14. The polar plots are divided into selected sun zenith angles (rows) and wavelengths (columns). The polar angle represents the azimuth (zero "looking at the sun"), while the radius represents the radiance propagation angle (same as the viewing zenith angle). The color represents the R_{rs} magnitude. The color scale among wavelengths for visualization purposes. For θ_s=60° specifically, some indicated slices are presented in 1D plots in Fig. 14. Section 1: sun's meridian plane. Section 2: perpendicular plane to the sun's meridian plane. Section 3: constant θ=60°.
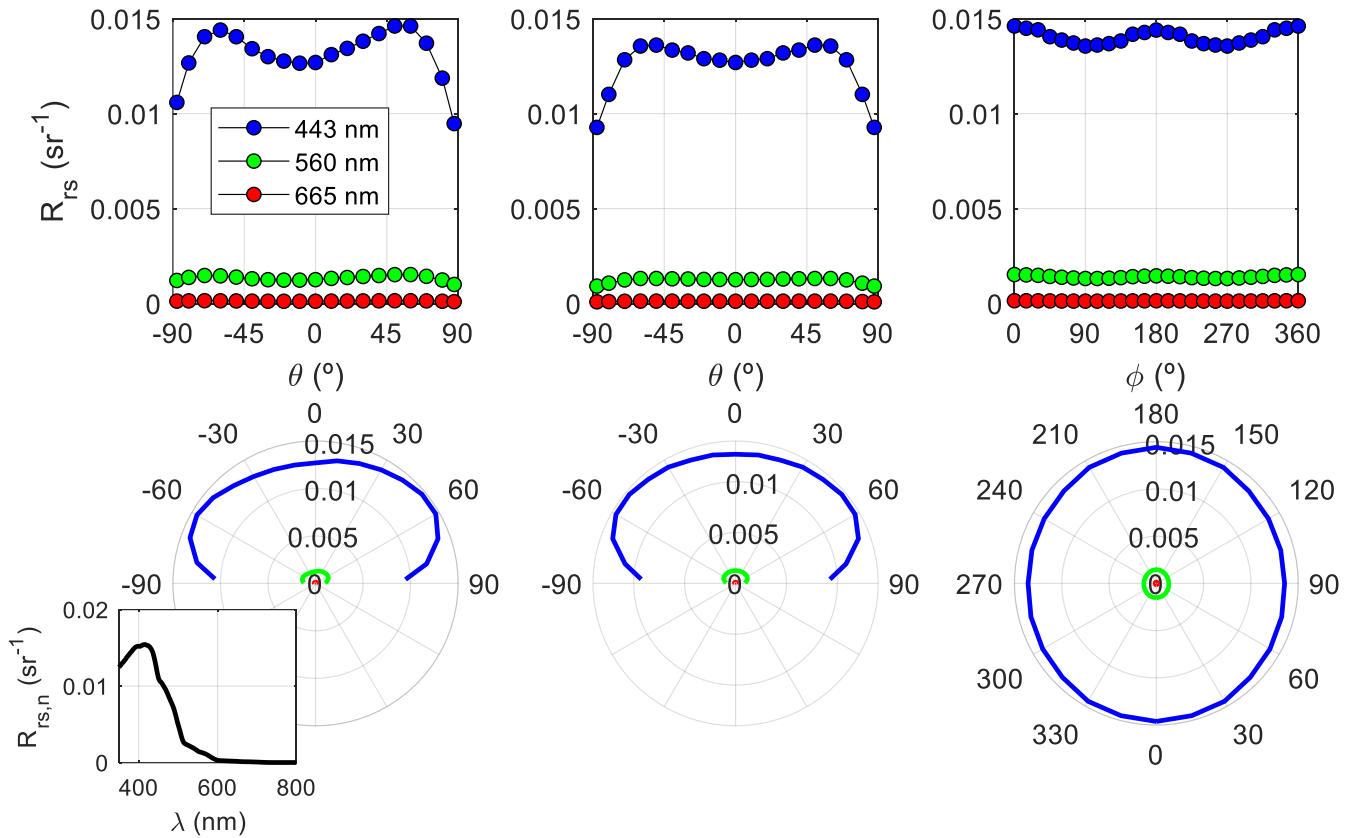
Figure 14 Angular variability of Hydrolight-simulated R_{rs} for the oligotrophic water case (spectrum shown in a corner). The plots represent the three sections for $\theta_s=60°$ in Fig. 13, in consecutive columns. Here, the sections are plotted in cartesian coordinates in the upper plots and polar coordinates in the lower ones.

775   Figs. 15 and 16 show an analog example for a productive water scenario. Notable is the azimuthal maximum shift to the $\phi = 180°$ direction. This is explained by the dominance of the particle phase function and the appearance of multiple scattering, which starts to become important even for small concentrations. This implies that the radiance at angle $\theta = -70°$ (or $\theta = 70°$ for $\phi = 180°$) is less influenced by the shape of the phase function at the particular direction given by the single scattering

780   direction. Instead, multiple scattering makes the resulting radiances influenced by the phase function in variable ranges reaching $\Psi < 120°$, where it increases sharply. Indeed, multiple scattering does not generate isotropy in R_{rs} as might be believed by some, but instead changes the angular pattern of the anisotropy. This behaviour, although already documented (Loisel and Morel, 2001), was somehow not assimilated by most within the community.
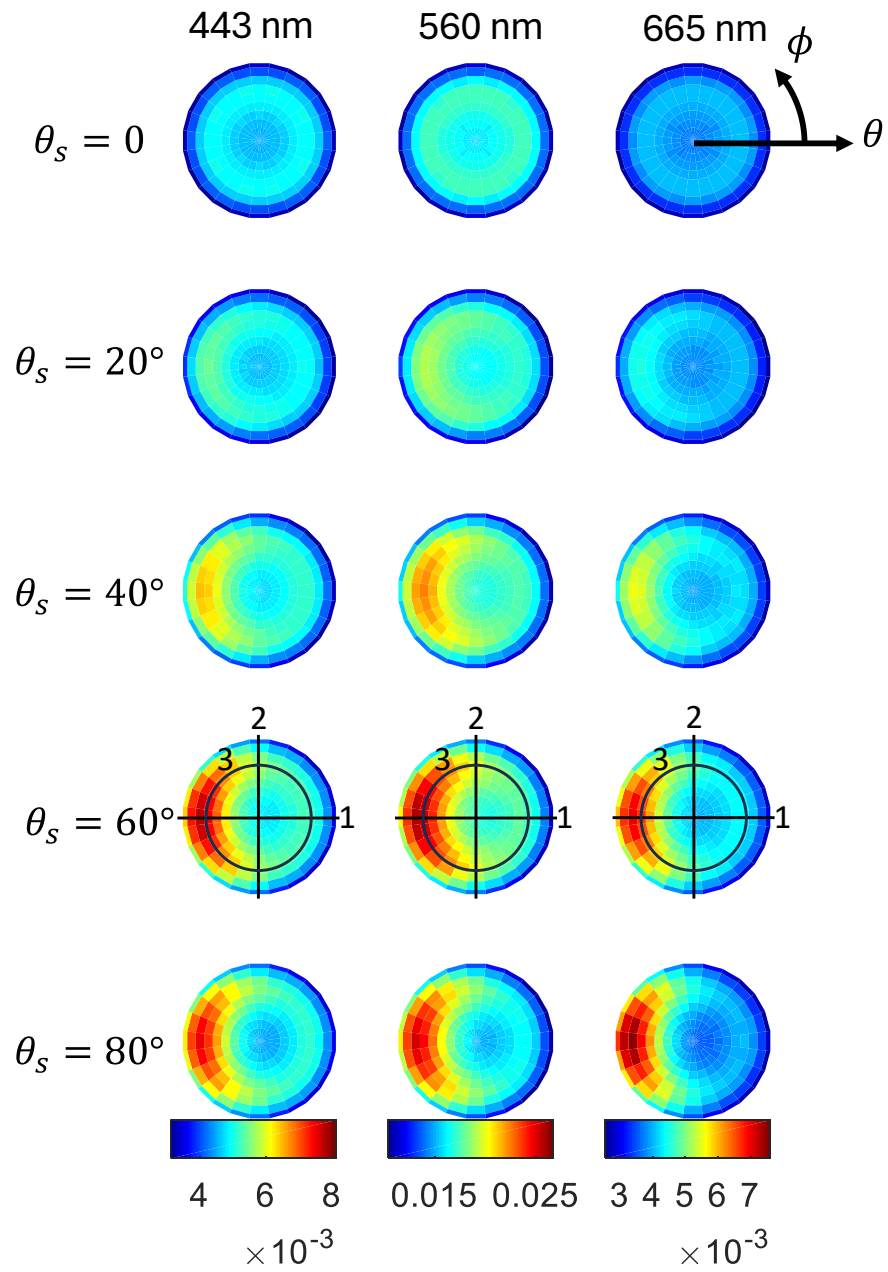
785

Figure 15 As in Fig. 13, but for the angular variability of R_{rs} for the productive water case.
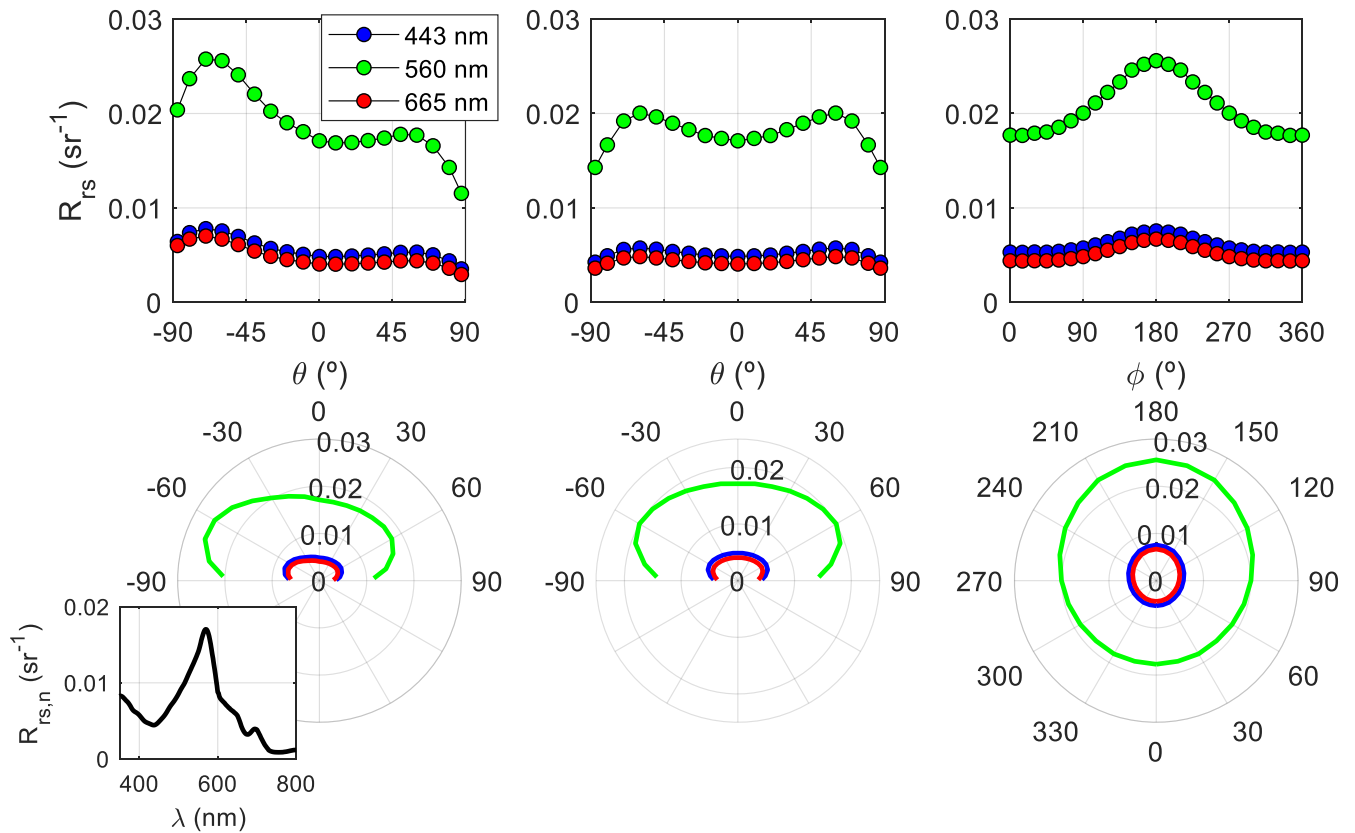
Figure 16 As in Fig. 14, but for the angular variability of R_{rs} for the productive water case.

4.5 Reflectance validation with in situ data

The number of relationships imposed to the IOPs, as well as the cross-checks among them give confidence on the realism of the SD generated. Yet, to be further confident that the synthetic AOPs represent natural waters, it is desirable to show some comparison to in situ data that involves the AOPs themselves.

We evaluated in Fig. 17 the R_{rs} (normalized geometry) of our entire SD through the spectral quality index (QWIP) by Dierssen et al. (2022). Such index aims at providing a quality estimate for a hyperspectral R_{rs}. QWIP was developed a large dataset of in situ R_{rs}, so this comparison can be seen as a comparison to real R_{rs} data. In Dierssen et al. (2022), it is mentioned that values within the 0.2 margins have high similarity to real spectra measured in the field, which for the case of the SD, is verified in 4993 out of the 5000 spectra. Still, these 7 spectra are close to the limit, and may simply contain some bio-optical characteristics that were not present in the QWIP calibration dataset. No spectra are clearly off from the

main trend line, thus giving confidence in the quality of our SD in terms of this index and of the data from which it was derived.
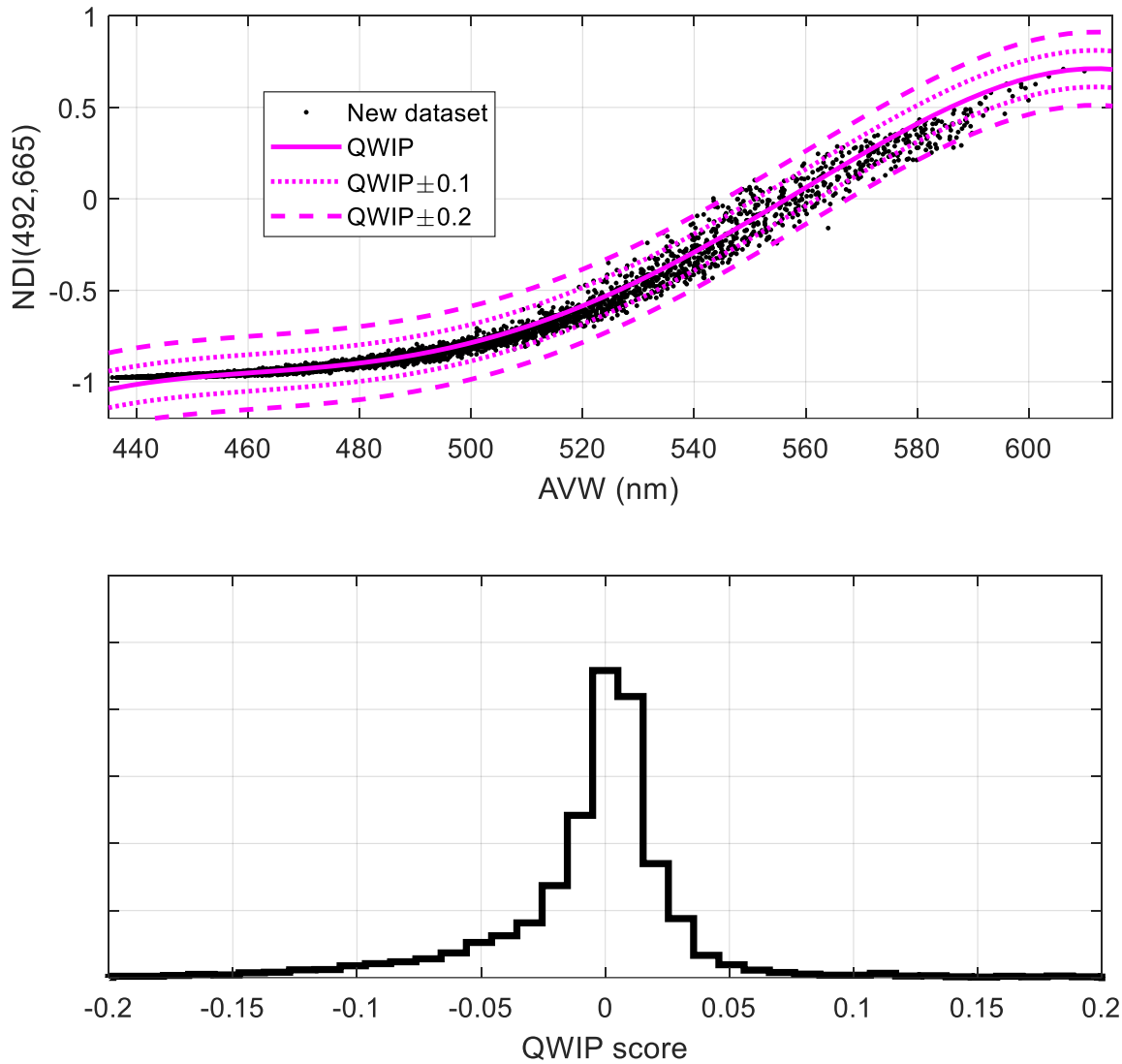
Figure 17 Upper plot: scatter plot between the apparent optical wavelength (Vandermeulen et al., 2020) and the NDI index: $NDI(492, 665) = \frac{R_{rs}(665)-R_{rs}(492)}{R_{rs}(665)+R_{rs}(492)}$. Magenta lines: QWIP score (Dierssen et al., 2022) and error bars. Lower plot: histogram of the QWIP score, defined as the difference respect to the QWIP curve.

Next assessment helps to verify the covariability between R_{rs} and the absorption coefficient. A one-dimensional predictor χ is derived from an R_{rs} (Lee et al., 2002), as in eq. (20):

$$\chi = \log_{10}\left(\frac{R_{rs}(443)+R_{rs}(490)}{R_{rs}(560)+5\frac{R_{rs}^2(665)}{R_{rs}(490)}}\right) \quad (20)$$

810 This χ index is matched to non-water absorption spectrum at 560 nm $a_{nw}(560)$. There are several open access, freely available in situ datasets that contain both measured variables matched together, such as Valente et al. (2022), Zibordi and Berthon (2024) and the PACE Schaeffer, Mouw and Biosope datasets (Casey et al., 2020). Fig. 18 clearly shows the excellent average overlap between our SD and measured data, besides differences due to the difficulties of measuring very low absorption. Different bio-optical

815 characteristics produce slight deviations from the mean trend, indicating natural variability.
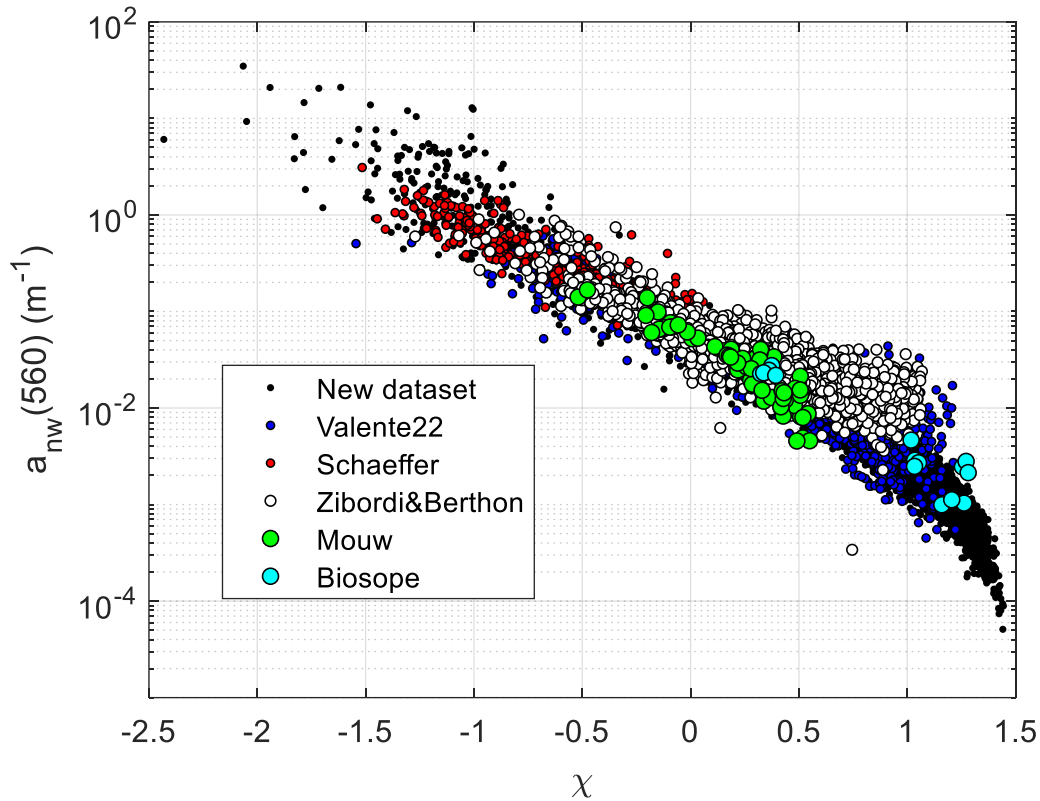
Figure 18 A scatter plot between the R_{rs}-generated χ index and the matched non-water absorption spectrum at 560 nm $a_{nw}(560)$. Black dots are from the SD and coloured dots are from field data from various references (see text).

820 A typical benchmark is shown next, where a given chlorophyll concentration in the SD is related to the generated R_{rs} through the maximum band ratio MBR_{OC4}, an index that is used to estimate chlorophyll in the ocean, defined in eq. (21):

$$MBR_{OC4} = \frac{\max [R_{rs}(443), R_{rs}(490), R_{rs}(510)]}{R_{rs}(560)} \quad (21)$$

This index has been also used to study the consistency of a given SD in all kinds of water (Nechad et al.,
825 2015). Here, matched MBR_{OC4} and chlorophyll concentration from two large in situ datasets are plotted (Valente et al., 2022;Zibordi and Berthon, 2024), showing a good general overlap, though with some degree of differences among them, that are explainable due to different bio-optical characteristics of the seas sampled (Szeto et al., 2011). Data from our SD generally agrees with the trend, that essentially shows high linearity in the middle section, while saturating at the extremes due to loss of sensitivity. The data
830 cloud of the SD also displays a spread that embraces the in situ datasets used for comparison, suggesting that the optical variability in the in situ datasets is well represented.
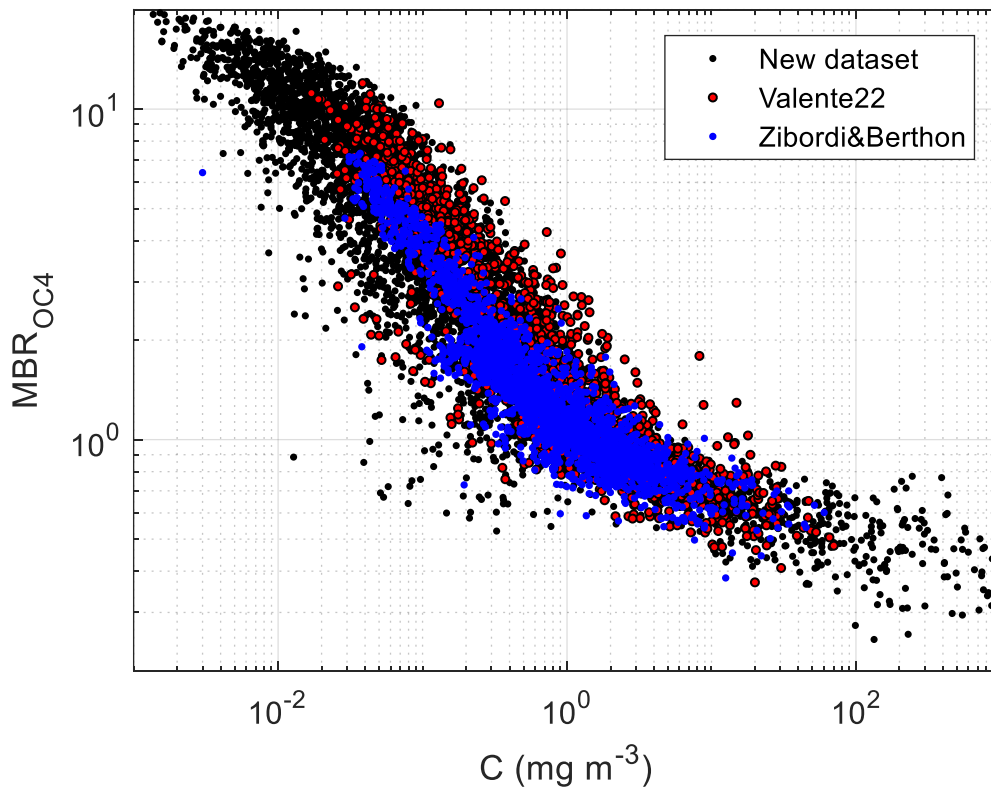
Figure 19 Chlorophyll concentration as a function of the maximum band ratio for OC4-type algorithms, for the SD and for data in Valente et al. (2022) and Zibordi and Berthon (2024).

The last comparison to real R_{rs} data involves the relationship to the total suspended matter concentration (T), a relevant parameter for coastal and inland water studies, which usually show higher turbidities. Interestingly, this involves the absolute value of R_{rs} and not ratios. In particular, it is known that T covaries with R_{rs} at long wavelengths, and 665 nm is commonly employed, due to the lesser disturbance by CDOM. Our SD does not use T for its generation, so the estimation $T = N + 0.07C$, after Brando and Dekker (2003). Fig. 20 shows that the new SD follows the same trend as that from in situ datasets (Valente et al., 2022;Zibordi and Berthon, 2024), but also displaying a level of spread that includes the in situ datasets, once more demonstrating the success in reproducing a range of natural variability.
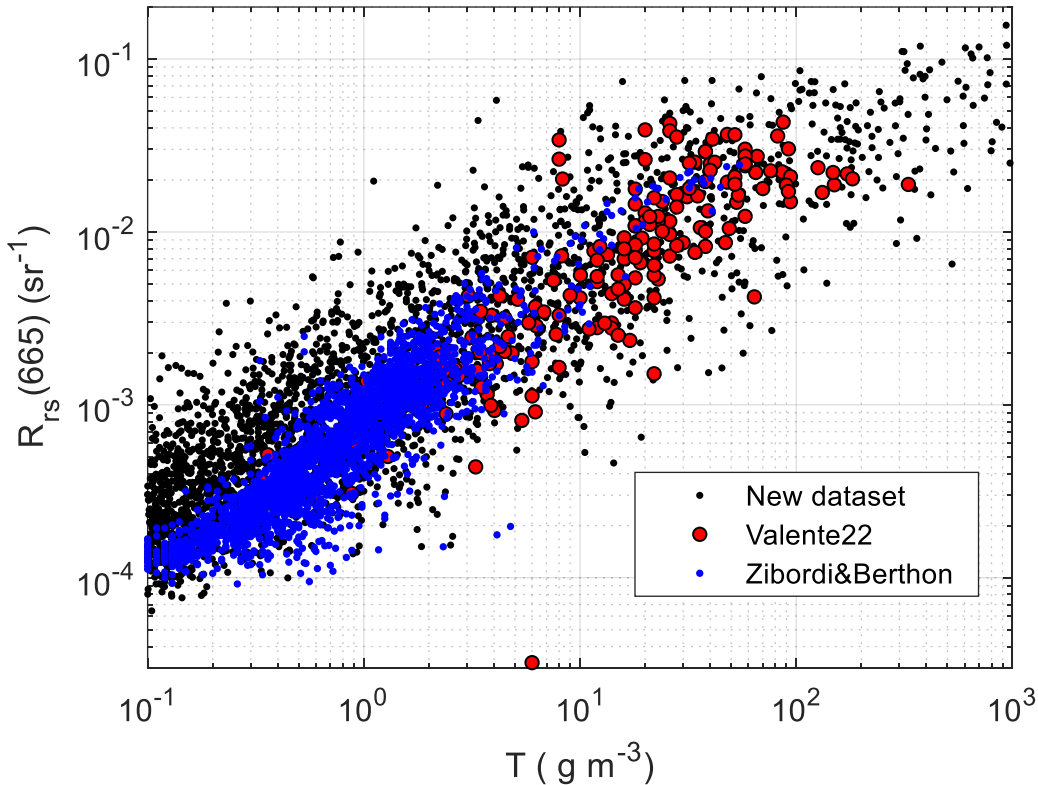
Figure 20 Total suspended matter concentration as a function of $R_{rs}(665)$, for the SD and for data in Valente et al. (2022) and Zibordi and Berthon (2024).

5. Data file description

Output data is organized in netCDF files, each containing a given IOP setup and all directional AOP output. Table 4 details the file structure. Variables have different sizes, according to their dependence on the following variables that can take the following number of different values: sun zenith angle θ_s, $n_s = 10$, zenithal direction of radiance propagation, θ, $n_\theta = 10$, azimuthal direction of radiance propagation ϕ, $n_\phi = 13$, wavelength of radiation in vacuum λ, $n_\lambda = 451$. All in-water AOPs refer to the zero depth, just below the surface. Diffuse attenuation coefficients instead required the choice of two depths approximate the depth derivatives, which were 0 m and 1 cm, as set by default in Hydrolight.

Table 4 File description

Parameter	Description	Units	Size
C	Chlorophyll concentration	mg m^{-3}	1x1
N	Non-algal particles concentration	g m^{-3}	1 x 1
Y	Light absorption coefficient of coloured dissolved organic matter at 440 nm	m^{-1}	1 x 1
theta_s	Sun zenith angle (zero at zenith)	°	n_s x 1
theta	Zenithal direction of radiance propagation (zero towards zenith)	°	n_θ x 1
phi	Azimuthal direction of radiance propagation (zero towards the sun)	°	n_ϕ x 1
lambda	Wavelength of radiation in vacuum	nm	n_λ x 1
Esdir_Es_ratio	Above-surface direct to total downwelling irradiance ratio	-	n_s x n_λ
aw	Spectral light absorption coefficient by seawater at 20 °C and S=35 PSU	m^{-1}	n_λ x 1
aph	Spectral light absorption coefficient by phytoplankton	m^{-1}	n_λ x 1

ay	Spectral light absorption coefficient by coloured dissolved organic matter	m^{-1}	n_λ x 1
aNAP	Spectral light absorption coefficient by non-algal particles	m^{-1}	n_λ x 1
bw	Spectral light scattering coefficient by seawater at 20 ºC and S=35 PSU	m^{-1}	n_λ x 1
bph	Spectral light scattering coefficient by phytoplankton	m^{-1}	n_λ x 1
bNAP	Spectral light scattering coefficient by non-algal particles	m^{-1}	n_λ x 1
bbw	Spectral light backscattering coefficient by seawater at 20 ºC and S=35 PSU	m^{-1}	n_λ x 1
bbph	Spectral light backscattering coefficient by phytoplankton	m^{-1}	n_λ x 1
bbNAP	Spectral light backscattering coefficient by non-algal particles	m^{-1}	n_λ x 1
Rrs	Spectral angle-dependent above-water remote sensing reflectance $\left(\frac{L_w}{E_s}\right)$	sr^{-1}	n_s x n_θ x n_ϕ x n_λ
rrs	Spectral angle-dependent underwater radiance reflectance $\left(\frac{L_u}{E_d}\right)$	sr^{-1}	n_s x n_θ x n_ϕ x n_λ
Q	Spectral angle-dependent underwater Q-factor $(\frac{E_u}{L_u})$	sr	n_s x n_θ x n_ϕ x n_λ
Kou	Spectral diffuse attenuation coefficient of scalar upwelling irradiance	m^{-1}	n_s x n_λ
Kod	Spectral diffuse attenuation coefficient of scalar downwelling irradiance	m^{-1}	n_s x n_λ

Ko	Spectral diffuse attenuation coefficient of scalar total (spherical) irradiance	m^{-1}	n_s x n_λ
Ku	Spectral diffuse attenuation coefficient of planar upwelling irradiance	m^{-1}	n_s x n_λ
Kd	Spectral diffuse attenuation coefficient of planar downwelling irradiance	m^{-1}	n_s x n_λ
Knet	Spectral diffuse attenuation coefficient of net planar irradiance	m^{-1}	n_s x n_λ
KLu	Spectral diffuse attenuation coefficient of upwelling radiance towards the zenith	m^{-1}	n_s x n_λ
mu_u	Spectral average cosine of the upwelling radiance	-	n_s x n_λ
mu_d	Spectral average cosine of the downwelling radiance	-	n_s x n_λ
mu_tot	Spectral average cosine of the total radiance	-	n_s x n_λ
R	Spectral underwater irradiance reflectance ($\frac{E_u}{E_d}$)	-	n_s x n_λ

6. Data availability

855

Data described in this manuscript freely accessible from Zenodo at https://doi.org/10.5281/zenodo.11637178 (Pitarch and Brando, 2024). The repository hosts two versions of the dataset: one hyperspectral, from 350 nm to 900 nm, in steps of 1 nm, and a smaller, multispectral on, for the twelve Sentinel 3-OLCI bands between 400 nm and 753 nm.

7. Conclusions

860

The presented dataset fills several gaps, as identified in our literature review of publicly available in situ and synthetic datasets. The large quantity and high quality of the in situ data allowed the application of

stringent quality control procedures to develop novel bio-optical relationships involving parameters that model absorption and scattering of the optically active constituents. The spread in the data clouds used for bio-optical modelling was reproduced as probability density functions, resulting in a realistic depiction of the natural variability of the in situ data. Validation exercises were provided for the remote-sensing reflectance, showing consistency with the benchmark in situ datasets for every example. Our dataset is therefore representative of natural waters of varying trophic levels and optical complexity. The underlying bio-optical relationships can be assumed to become a reference for future optical studies.

Apparent optical properties are resolved at all geometric angles available by the radiative transfer simulations, making this one the first directional dataset ever published. This detail makes it suitable for directional studies of reflectance, diffuse attenuation and any other derived quantity. The dataset, in its hyperspectral and multi-angular format, is relevant for bio-optical and directional studies applied to current satellite-borne sensors such as OLCI, and as well as to next-generation missions such as PACE and CHIME.

The synthetic dataset is distributed in netCDF format as single files for every IOP case, enabling efficient space management, as well as straightforward handling with software packages. Despite the very fine spectral step of 1 nm between 350 nm and 800 nm and that each file contains the IOP setup as well as all directional AOPs for all 1300 angular configurations (and hemispheric variables such as K_d are included for all 10 sun zenith angles), each of the 5000 files only weights approximately 5700 kB.

8. Author contribution

J.P., V.E.B: Conceptualization of the study, development or design of methodology, validation, Writing – review & editing. J.P.: Data curation, Formal analysis, Software, Visualization, Writing – original draft preparation. V.E.B.: Funding acquisition, Project administration.

9. Competing interests

The authors declare that they have no conflict of interest.

10. Acknowledgements

We are grateful to Davide d'Alimonte, Tamito Kajiyama, Constant Mazeran and Marco Talone for carrying out independent analyses with previous versions of this dataset, that were fundamental to develop it to its final configuration. Flavio la Padula and Vega Forneris assisted with IT requirements. Curtis Mobley, Juan Ignacio Gossn, Giuseppe Zibordi, David McKee and Reviewer 1 are thanked for proving valuable comments and suggestions on a previous version of the manuscript that helped to improve its quality.

This study was carried out in the frame of the Copernicus study "BRDF correction of S3 OLCI water reflectance products" (contract No.RB_EUM-CO-21-4600002626-JIG), conducted by EUMETSAT. The work also acknowledges the support of the Ocean Colour Thematic Assembly Centre of the Copernicus Marine Environment and Monitoring Service (contract: 21001L02-COP-TAC OC-2200–Lot 2: Provision of Ocean Colour Observation Products (OC-TAC)). J.P. thanks financial support by the EU - Next Generation EU Mission 4 "Education and Research" - Project IR0000032 – ITINERIS - Italian Integrated Environmental Research Infrastructures System - CUP B53C22002150006.

References

Astoreca, R., Doxaran, D., Ruddick, K., Rousseau, V., and Lancelot, C.: Influence of suspended particle concentration, composition and size on the variability of inherent optical properties of the Southern North Sea, Continental Shelf Research, 35, 117-128, https://doi.org/10.1016/j.csr.2012.01.007, 2012.

Aurin, D. A., Dierssen, H. M., Twardowski, M. S., and Roesler, C. S.: Optical complexity in Long Island Sound and implications for coastal ocean color remote sensing, Journal of Geophysical Research: Oceans, 115, https://doi.org/10.1029/2009JC005837, 2010.

Babin, M., Stramski, D., Ferrari, G. M., Claustre, H., Bricaud, A., Obolensky, G., and Hoepffner, N.: Variations in the light absorption coefficients of phytoplankton, nonalgal particles, and dissolved organic matter in coastal waters around Europe, Journal of Geophysical Research: Oceans, 108, https://doi.org/10.1029/2001JC000882, 2003.

Bengil, F., McKee, D., Beşiktepe, S. T., Sanjuan Calzado, V., and Trees, C.: A bio-optical model for integration into ecosystem models for the Ligurian Sea, Progress in Oceanography, 149, 1-15, https://doi.org/10.1016/j.pocean.2016.10.007, 2016.

915 Bernard, S., Probyn, T. A., and Quirantes, A.: Simulating the optical properties of phytoplankton cells using a two-layered spherical geometry, Biogeosciences Discuss., 2009, 1497-1563, 10.5194/bgd-6-1497-2009, 2009.

Blondeau-Patissier, D., Brando, V. E., Oubelkheir, K., Dekker, A. G., Clementson, L. A., and Daniel, P.: Bio-optical variability of the absorption and scattering properties of the Queensland inshore and reef 920 waters, Australia, Journal of Geophysical Research: Oceans, 114, https://doi.org/10.1029/2008JC005039, 2009.

Blondeau-Patissier, D., Schroeder, T., Clementson, L. A., Brando, V. E., Purcell, D., Ford, P., Williams, D. K., Doxaran, D., Anstee, J., Thapar, N., and Tovar-Valencia, M.: Bio-Optical Properties of Two Neigboring Coastal Regions of Tropical Northern Australia: The Van Diemen Gulf and Darwin Harbour, 925 Front. Mar. Sci., 4, 10.3389/fmars.2017.00114, 2017.

Bracher, A.: Phytoplankton pigment concentrations in the Southern Ocean during RV POLARSTERN cruise PS103 in Dec 2016 to Jan 2017. In: Supplement to: Álvarez, Eva; Thoms, Silke; Bracher, Astrid; Liu, Y; Völker, Christoph (2019): Modeling Photoprotection at Global Scale: The Relative Role of Nonphotosynthetic Pigments, Physiological State, and Species Composition. Global Biogeochemical 930 Cycles, 33(7), 904-926, https://doi.org/10.1029/2018GB006101, PANGAEA, 2019.

Bracher, A., and Liu, Y.: Spectrophotometric measurements of absorption coefficients by non-algal particles in the Atlantic Southern Ocean during RV POLARSTERN cruise PS103 in Dec 2016 to Jan 2017. PANGAEA, 2021.

Bracher, A., Liu, Y., Hellmann, S., and Röttgers, R.: Absorption coefficients by coloured dissolved 935 organic matter from North Sea to Fram Strait measured underway with a Liquid Waveguide Capillary Cell system during POLARSTERN cruise PS99.1. PANGAEA, 2021a.

Bracher, A., Liu, Y., Oelker, J., and Röttgers, R.: Absorption coefficients by coloured dissolved organic matter across the South Atlantic Ocean measured underway with a Liquid Waveguide Capillary Cell system during POLARSTERN cruise PS103. PANGAEA, 2021b.

940 Bracher, A., Liu, Y., and Wiegmann, S.: Spectrophotometric measurements of absorption coefficients by phytoplankton during HEINCKE cruise HE462 in the North Sea and Sogne Fjord from 29 April to 7 May 2016. PANGAEA, 2021c.

Bracher, A., Liu, Y., and Wiegmann, S.: Spectrophotometric measurements of absorption coefficients by non-algal particles during during HEINCKE cruise HE462 in the North Sea and Sogne Fjord from 29 945 April to 7 May 2016. PANGAEA, 2021d.

Bracher, A., Liu, Y., and Wiegmann, S.: Spectrophotometric measurements of absorption coefficients by non-algal particles during RV POLARSTERN cruise PS121 from 11 Aug to 10 Sep 2019. PANGAEA, 2021e.

Bracher, A., Liu, Y., and Wiegmann, S.: Spectrophotometric measurements of absorption coefficients by 950 phytoplankton during RV POLARSTERN cruise PS121 from 11 Aug to 10 Sep 2019. PANGAEA, 2021f.

Bracher, A., Liu, Y., Wiegmann, S., and Röttgers, R.: Absorption coefficients by coloured dissolved organic matter obtained underway with a Liquid Waveguide Capillary Cell system during HEINCKE cruise HE462 in the North Sea and Sogne Fjord. PANGAEA, 2021g.

Bracher, A., Liu, Y., Wiegmann, S., and Röttgers, R.: Absorption coefficients by coloured dissolved 955 organic matter (CDOM) from North Sea to Fram Strait measured at fixed stations with a Liquid Waveguide Capillary Cell system during POLARSTERN cruise PS121. PANGAEA, 2021h.

Bracher, A., Liu, Y., Wiegmann, S., Xi, H., and Röttgers, R.: Absorption coefficients by coloured dissolved organic matter across the Atlantic Ocean measured underway with a Liquid Waveguide Capillary Cell system during POLARSTERN cruise PS113. PANGAEA, 2021i.

960   Bracher, A., Liu, Y., Xi, H., and Wiegmann, S.: Spectrophotometric measurements of absorption coefficients by non-algal particles during POLARSTERN cruise PS113 along an Atlantic Transect. PANGAEA, 2021j.

Bracher, A., Liu, Y., Xi, H., and Wiegmann, S.: Spectrophotometric measurements of absorption coefficients by phytoplankton during POLARSTERN cruise PS113 along an Atlantic Transect.
965   PANGAEA, 2021k.

Bracher, A., and Taylor, B. B.: Phytoplankton absorption during POLARSTERN cruise ANT-XXVI/4 (PS75). PANGAEA, 2021.

Bracher, A., Taylor, B. B., and Cheah, W.: Phytoplankton absorption during SONNE cruise SO218. PANGAEA, 2021l.

970   Brando, V. E., and Dekker, A. G.: Satellite hyperspectral remote sensing for estimating estuarine and coastal water quality, IEEE Transactions on Geoscience and Remote Sensing, 41, 1378-1387, 10.1109/TGRS.2003.812907, 2003.

Brando, V. E., Dekker, A. G., Park, Y. J., and Schroeder, T.: Adaptive semianalytical inversion of ocean color radiometry in optically complex waters, Applied Optics, 51, 2808-2833, 10.1364/AO.51.002808,
975   2012.

Brewin, R. J. W., Dall'Olmo, G., Sathyendranath, S., and Hardman-Mountford, N. J.: Particle backscattering as a function of chlorophyll and phytoplankton size structure in the open-ocean, Opt. Express, 20, 17632-17652, 10.1364/OE.20.017632, 2012.

Bricaud, A., Babin, M., Morel, A., and Claustre, H.: Variability in the chlorophyll-specific absorption
980   coefficients of natural phytoplankton: Analysis and parameterization, J. Geophys. Res., 100, 13321, 10.1029/95JC00463, 1995.

Bricaud, A., Morel, A., Babin, M., Allali, K., and Claustre, H.: Variations of light absorption by suspended particles with chlorophyll *a* concentration in oceanic (case 1) waters: Analysis and implications for bio-optical models, Journal of Geophysical Research: Oceans, 103, 31033-31044, 10.1029/98JC02712, 1998.

Casey, K. A., Rousseaux, C. S., Gregg, W. W., Boss, E., Chase, A. P., Craig, S. E., Mouw, C. B., Reynolds, R. A., Stramski, D., Ackleson, S. G., Bricaud, A., Schaeffer, B., Lewis, M. R., and Maritorena, S.: A global compilation of in situ aquatic high spectral resolution inherent and apparent optical property data for remote sensing applications, Earth Syst. Sci. Data, 12, 1123-1139, 10.5194/essd-12-1123-2020, 2020.

Castagna, A., Amadei Martínez, L., Bogorad, M., Daveloose, I., Dasseville, R., Dierssen, H. M., Beck, M., Mortelmans, J., Lavigne, H., Dogliotti, A., Doxaran, D., Ruddick, K., Vyverman, W., and Sabbe, K.: Optical and biogeochemical properties of diverse Belgian inland and coastal waters, Earth Syst. Sci. Data, 14, 2697-2719, 10.5194/essd-14-2697-2022, 2022.

Chami, M., Lafrance, B., Fougnie, B., Chowdhary, J., Harmel, T., and Waquet, F.: OSOAA: a vector radiative transfer model of coupled atmosphere-ocean system for a rough sea surface application to the estimates of the directional variations of the water leaving reflectance to better process multi-angular satellite sensors data over the ocean, Opt. Express, 23, 27829-27852, 10.1364/OE.23.027829, 2015.

Cherukuru, N., Davies, P. L., Brando, V. E., Anstee, J. M., Baird, M. E., Clementson, L. A., and Doblin, M. A.: Physical oceanographic processes influence bio-optical properties in the Tasman Sea, Journal of Sea Research, 110, 1-7, https://doi.org/10.1016/j.seares.2016.01.008, 2016.

Churilova, T., Moiseeva, N., Skorokhod, E., Efimova, T., Buchelnikov, A., Artemiev, V., and Salyuk, P.: Parameterization of Light Absorption of Phytoplankton, Non-Algal Particles and Coloured Dissolved Organic Matter in the Atlantic Region of the Southern Ocean (Austral Summer of 2020), Remote Sensing, 15, 634, 2023.

D'Alimonte, D., Zibordi, G., Kajiyama, T., and Cunha, J. C.: Monte Carlo code for high spatial resolution ocean color simulations, Applied Optics, 49, 4936-4950, 10.1364/AO.49.004936, 2010.

Dierssen, H. M., Vandermeulen, R. A., Barnes, B. B., Castagna, A., Knaeps, E., and Vanhellemont, Q.: QWIP: A Quantitative Metric for Quality Control of Aquatic Reflectance Spectral Shape Using the Apparent Visible Wavelength, Frontiers in Remote Sensing, 3, 10.3389/frsen.2022.869611, 2022.

Doerffer, R., and Schiller, H.: The MERIS Case 2 water algorithm, International Journal of Remote Sensing, 28, 517-535, 10.1080/01431160600821127, 2007.

Fournier, G. R., and Forand, J. L.: Analytic phase function for ocean water, Ocean Optics XII, 1994, 194-201,

Gonçalves-Araujo, R., Wiegmann, S., and Bracher, A.: Absorption coefficient spectra of non-algal particles during POLARSTERN cruise ARK-XXVI/3 (PS78, TRANSARC). In: In supplement to: Gonçalves-Araujo, Rafael; Rabe, Benjamin; Peeken, Ilka; Bracher, Astrid (2018): High colored dissolved organic matter (CDOM) absorption in surface waters of the central-eastern Arctic Ocean: Implications for biogeochemistry and ocean color algorithms. PLoS ONE, 13(1), e0190838, https://doi.org/10.1371/journal.pone.0190838, PANGAEA, 2018.

Gons, H. J., Burger-Wiersma, T., Otten, J. H., and Rijkeboer, M.: Coupling of phytoplankton and detritus in a shallow, eutrophic lake (Lake Loosdrecht, The Netherlands), in: Restoration and Recovery of Shallow Eutrophic Lake Ecosystems in The Netherlands, Dordrecht, 1992, 51-59,

Gregg, W. W., and Carder, K. L.: A simple spectral solar irradiance model for cloudless maritime atmospheres, Limnol. Oceanogr., 35, 1657-1675, 10.4319/lo.1990.35.8.1657, 1990.

Harrison, A. W., and Coombes, C. A.: Angular distribution of clear sky short wavelength radiance, Solar Energy, 40, 57-63, 1988.

He, S., Zhang, X., Xiong, Y., and Gray, D.: A Bidirectional Subsurface Remote Sensing Reflectance Model Explicitly Accounting for Particle Backscattering Shapes, Journal of Geophysical Research: Oceans, 122, 8614-8626, 10.1002/2017JC013313, 2017.

Hölemann, J. A., Koch, B. P., Juhls, B., and Timokhov, L.: Colored dissolved organic matter (CDOM) and dissolved organic carbon (DOC) measured during cruise TRANSDRIFT-XXII, Laptev Sea. PANGAEA, 2020.

IOCCG: Remote Sensing of Inherent Optical Properties: Fundamentals, Tests of Algorithms, and Applications, International Ocean-Colour Coordinating Group, IOCCG, Dartmouth, Canada5, 1-122, 2006.

Juhls, B., Kattner, G., and Skorospekhova, T.: Surface water Dissolved Organic Matter (CDOM) in the Lena River (2013). In: In supplement to: Juhls, Bennet; Overduin, Pier Paul; Hölemann, Jens A; Hieronymi, Martin; Matsuoka, Atsushi; Heim, Birgit; Fischer, Jürgen (2019): Dissolved organic matter at the fluvial–marine transition in the Laptev Sea using in situ data and ocean colour remote sensing. Biogeosciences, 16(13), 2693-2713, https://doi.org/10.5194/bg-16-2693-2019, PANGAEA, 2019.

Lain, L. R., Kravitz, J., Matthews, M., and Bernard, S.: Simulated Inherent Optical Properties of Aquatic Particles using The Equivalent Algal Populations (EAP) model, Scientific Data, 10, 412, 10.1038/s41597-023-02310-z, 2023.

Le, C., Hu, C., English, D., Cannizzaro, J., Chen, Z., Kovach, C., Anastasiou, C. J., Zhao, J., and Carder, K. L.: Inherent and apparent optical properties of the complex estuarine waters of Tampa Bay: What controls light?, Estuarine, Coastal and Shelf Science, 117, 54-69, https://doi.org/10.1016/j.ecss.2012.09.017, 2013.

Le, C., Lehrter, J. C., Hu, C., Schaeffer, B., MacIntyre, H., Hagy, J. D., and Beddick, D. L.: Relation between inherent optical properties and land use and land cover across Gulf Coast estuaries, Limnol. Oceanogr., 60, 920-933, https://doi.org/10.1002/lno.10065, 2015.

Lee, Z., Carder, K. L., and Arnone, R. A.: Deriving inherent optical properties from water color: a multiband quasi-analytical algorithm for optically deep waters, Applied Optics, 41, 5755, 10.1364/AO.41.005755, 2002.

1055 Lee, Z., Hu, C., Shang, S., Du, K., Lewis, M., Arnone, R., and Brewin, R.: Penetration of UV-visible solar radiation in the global oceans: Insights from ocean color remote sensing, Journal of Geophysical Research: Oceans, 118, 4241-4255, 10.1002/jgrc.20308, 2013.

Lee, Z. P., Du, K., Voss, K. J., Zibordi, G., Lubac, B., Arnone, R., and Weidemann, A.: An inherent-optical-property-centered approach to correct the angular effects in water-leaving radiance, Applied
1060 Optics, 50, 3155, 10.1364/AO.50.003155, 2011.

Liu, Y., Wiegmann, S., and Bracher, A.: Absorption coefficient spectra (median) of non-algal particles during POLARSTERN cruise PS99. In: In supplement to: Liu, Yangyang; Boss, Emmanuel; Chase, Alison P; Xi, Hongyan; Zhang, Xiaodong; Röttgers, Rüdiger; Pan, Yanqun; Bracher, Astrid (2019): Retrieval of phytoplankton pigments from underway spectrophotometry in the Fram Strait. Remote
1065 Sensing, 11(3), 318, https://doi.org/10.3390/rs11030318, PANGAEA, 2019a.

Liu, Y., Wiegmann, S., and Bracher, A.: Absorption coefficient spectra (median) of phytoplankton during POLARSTERN cruise PS99. In: In supplement to: Liu, Yangyang; Boss, Emmanuel; Chase, Alison P; Xi, Hongyan; Zhang, Xiaodong; Röttgers, Rüdiger; Pan, Yanqun; Bracher, Astrid (2019): Retrieval of phytoplankton pigments from underway spectrophotometry in the Fram Strait. Remote Sensing, 11(3),
1070 318, https://doi.org/10.3390/rs11030318, PANGAEA, 2019b.

Liu, Y., Wiegmann, S., and Bracher, A.: Absorption coefficient spectra (median) of phytoplankton during POLARSTERN cruise PS107. In: In supplement to: Liu, Yangyang; Boss, Emmanuel; Chase, Alison P; Xi, Hongyan; Zhang, Xiaodong; Röttgers, Rüdiger; Pan, Yanqun; Bracher, Astrid (2019): Retrieval of phytoplankton pigments from underway spectrophotometry in the Fram Strait. Remote Sensing, 11(3),
1075 318, https://doi.org/10.3390/rs11030318, In supplement to: Liu, Yangyang; Boss, Emmanuel; Chase, Alison P; Xi, Hongyan; Zhang, Xiaodong; Röttgers, Rüdiger; Pan, Yanqun; Bracher, Astrid (2019):

Retrieval of phytoplankton pigments from underway spectrophotometry in the Fram Strait. Remote Sensing, 11(3), 318, https://doi.org/10.3390/rs11030318, 2019c.

Liu, Y., Wiegmann, S., and Bracher, A.: Absorption coefficient spectra (median) of non-algal particles during POLARSTERN cruise PS107. In: In supplement to: Liu, Yangyang; Boss, Emmanuel; Chase, Alison P; Xi, Hongyan; Zhang, Xiaodong; Röttgers, Rüdiger; Pan, Yanqun; Bracher, Astrid (2019): Retrieval of phytoplankton pigments from underway spectrophotometry in the Fram Strait. Remote Sensing, 11(3), 318, https://doi.org/10.3390/rs11030318, 2019d.

Loisel, H., and Morel, A.: Light scattering and chlorophyll concentration in case 1 waters: A reexamination, Limnol. Oceanogr., 43, 847-858, 10.4319/lo.1998.43.5.0847, 1998.

Loisel, H., and Morel, A.: Non-isotropy of the upward radiance field in typical coastal (Case 2) waters, International Journal of Remote Sensing, 22, 275-295, 10.1080/014311601449934, 2001.

Loisel, H., Jorge, D. S. F., Reynolds, R. A., and Stramski, D.: A synthetic optical database generated by radiative transfer simulations in support of studies in ocean optics and optical remote sensing of the global ocean, Earth Syst. Sci. Data, 15, 3711-3731, 10.5194/essd-15-3711-2023, 2023.

Martinez-Vicente, V., Land, P. E., Tilstone, G. H., Widdicombe, C., and Fishwick, J. R.: Particulate scattering and backscattering related to water constituents and seasonal changes in the Western English Channel, Journal of Plankton Research, 32, 603-619, 10.1093/plankt/fbq013, 2010.

Mason, J. D., Cone, M. T., and Fry, E. S.: Ultraviolet (250–550 nm) absorption spectrum of pure water, Applied Optics, 55, 7163-7172, 10.1364/AO.55.007163, 2016.

Massicotte, P., Babin, M., Fell, F., Fournier-Sicre, V., and Doxaran, D.: The Coastal Surveillance Through Observation of Ocean Color (COASTℓOOC) dataset, Earth Syst. Sci. Data, 15, 3529-3545, 10.5194/essd-15-3529-2023, 2023.

Matthews, M. W., and Bernard, S.: Characterizing the Absorption Properties for Remote Sensing of Three Small Optically-Diverse South African Reservoirs, Remote Sensing, 5, 4370-4404, 2013.

Mobley, C. D., Gentili, B., Gordon, H. R., Jin, Z., Kattawar, G. W., Morel, A., Reinersman, P., Stamnes, K., and Stavn, R. H.: Comparison of numerical models for computing underwater light fields, Applied Optics, 32, 7484-7504, 10.1364/AO.32.007484, 1993.

Mobley, C. D.: Light and Water. Radiative Transfer in Natural Waters, Academic Press, 1994.

Mobley, C. D., Sundman, L. K., and Boss, E.: Phase function effects on oceanic light fields, Applied Optics, 41, 1035, 10.1364/AO.41.001035, 2002.

Moradi, M., and Arabi, B.: Seasonal and spatial variability in bio-optical properties of the Persian Gulf: Implications for ocean color remote sensing, Continental Shelf Research, 266, 105094, https://doi.org/10.1016/j.csr.2023.105094, 2023.

Morel, A., and Gentili, B.: Diffuse reflectance of oceanic waters II Bidirectional aspects, Applied Optics, 32, 6864, 10.1364/AO.32.006864, 1993.

Morel, A., and Gentili, B.: Diffuse reflectance of oceanic waters III Implication of bidirectionality for the remote-sensing problem, Applied Optics, 35, 4850, 10.1364/AO.35.004850, 1996.

Morel, A., and Maritorena, S.: Bio-optical properties of oceanic waters: A reappraisal, Journal of Geophysical Research: Oceans, 106, 7163-7180, 10.1029/2000JC000319, 2001.

Morel, A., Antoine, D., and Gentili, B.: Bidirectional reflectance of oceanic waters: accounting for Raman emission and varying particle scattering phase function, Applied Optics, 41, 6289, 10.1364/AO.41.006289, 2002.

Morel, A.: Are the empirical relationships describing the bio-optical properties of case 1 waters consistent and internally compatible?, Journal of Geophysical Research: Oceans, 114, https://doi.org/10.1029/2008JC004803, 2009.

Nechad, B., Ruddick, K., Schroeder, T., Oubelkheir, K., Blondeau-Patissier, D., Cherukuru, N., Brando, V., Dekker, A., Clementson, L., Banks, A. C., Maritorena, S., Werdell, P. J., Sá, C., Brotas, V., Caballero de Frutos, I., Ahn, Y. H., Salama, S., Tilstone, G., Martinez-Vicente, V., Foley, D., McKibben, M., Nahorniak, J., Peterson, T., Siliò-Calzada, A., Röttgers, R., Lee, Z., Peters, M., and Brockmann, C.: CoastColour Round Robin data sets: a database to evaluate the performance of algorithms for the retrieval of water quality parameters in coastal waters, Earth Syst. Sci. Data, 7, 319-348, 10.5194/essd-7-319-2015, 2015.

Oubelkheir, K., Ford, P. W., Cherukuru, N., Clementson, L. A., Petus, C., Devlin, M., Schroeder, T., and Steven, A. D. L.: Impact of a Tropical Cyclone on Terrestrial Inputs and Bio-Optical Properties in Princess Charlotte Bay (Great Barrier Reef Lagoon), Remote Sensing, 15, 652, 2023.

Park, Y.-J., and Ruddick, K.: Model of remote-sensing reflectance including bidirectional effects for case 1 and case 2 waters, Applied Optics, 44, 1236-1249, 10.1364/AO.44.001236, 2005.

Petit, T., Hamre, B., Sandven, H., Röttgers, R., Kowalczuk, P., Zablocka, M., and Granskog, M. A.: Inherent optical properties of dissolved and particulate matter in an Arctic fjord (Storfjorden, Svalbard) in early summer, Ocean Sci., 18, 455-468, 10.5194/os-18-455-2022, 2022.

Pitarch, J., and Brando, V.: A hyperspectral and multi-angular synthetic dataset of optical properties for waters with varying trophic levels and optical complexity. Zenodo, 2024.

Poulin, C., Zhang, X., Yang, P., and Huot, Y.: Diel variations of the attenuation, backscattering and absorption coefficients of four phytoplankton species and comparison with spherical, coated spherical and hexahedral particle optical models, Journal of Quantitative Spectroscopy and Radiative Transfer, 217, 288-304, https://doi.org/10.1016/j.jqsrt.2018.05.035, 2018.

Pykäri, J.: Absorption measurements of colored dissolved organic matter (cDOM) in Pohjanpitäjänlahti bay in May 2021. In: In: Pykäri, J (2022): Light attenuation data set along a coastal salinity gradient in Pohjanpitäjänlahti bay in May 2021. PANGAEA, https://doi.org/10.1594/PANGAEA.947091, PANGAEA, 2022.

Roettgers, R., McKee, D., and Utschig, C.: Temperature and salinity correction coefficients for light absorption by water in the visible to infrared spectral region, Opt. Express, 22, 25093-25108, 10.1364/OE.22.025093, 2014.

1150 Roettgers, R., Doerffer, R., McKee, D., and Schonfeld, W.: Algorithm Theoretical Basis Document The Water Optical Properties Processor (WOPP). Pure water spectral absorption, scattering, and real part of refractive index model, Helmholtz-Zentrum Geesthacht, University of Strathclyde, ESA/ESRIN, 20, 2016.

Rozanov, V. V., Rozanov, A. V., Kokhanovsky, A. A., and Burrows, J. P.: Radiative transfer through 1155 terrestrial atmosphere and ocean: Software package SCIATRAN, Journal of Quantitative Spectroscopy and Radiative Transfer, 133, 13-71, https://doi.org/10.1016/j.jqsrt.2013.07.004, 2014.

Soppa, M. A., Dinter, T., Taylor, B. B., and Bracher, A.: Phytoplankton absorption during POLARSTERN cruise ANT-XXVIII/3. In: In supplement to: Soppa, MA et al. (2013): Satellite derived euphotic depth in the Southern Ocean: Implications for primary production modelling. Remote Sensing 1160 of Environment, 137, 198-211, https://doi.org/10.1016/j.rse.2013.06.017, PANGAEA, 2013a.

Soppa, M. A., Dinter, T., Taylor, B. B., and Bracher, A.: Particulate absorption during POLARSTERN cruise ANT-XXVIII/3. In: In supplement to: Soppa, MA et al. (2013): Satellite derived euphotic depth in the Southern Ocean: Implications for primary production modelling. Remote Sensing of Environment, 137, 198-211, https://doi.org/10.1016/j.rse.2013.06.017, PANGAEA, 2013b.

1165 Sullivan, J. M., and Twardowski, M. S.: Angular shape of the oceanic particulate volume scattering function in the backward direction, Applied Optics, 48, 6811, 10.1364/AO.48.006811, 2009.

Szeto, M., Werdell, P. J., Moore, T. S., and Campbell, J. W.: Are the world's oceans optically different?, Journal of Geophysical Research: Oceans, 116, https://doi.org/10.1029/2011JC007230, 2011.

Talone, M., Zibordi, G., and Pitarch, J.: On the Application of AERONET-OC Multispectral Data to Assess Satellite-Derived Hyperspectral Rrs, IEEE Geosci. Remote Sensing Lett., 21, 1-5, 10.1109/LGRS.2024.3350928, 2024.

Tilstone, G. H., Peters, S. W. M., van der Woerd, H. J., Eleveld, M. A., Ruddick, K., Schönfeld, W., Krasemann, H., Martinez-Vicente, V., Blondeau-Patissier, D., Röttgers, R., Sørensen, K., Jørgensen, P. V., and Shutler, J. D.: Variability in specific-absorption properties and their use in a semi-analytical ocean colour algorithm for MERIS in North Sea and Western English Channel Coastal Waters, Remote Sensing of Environment, 118, 320-338, https://doi.org/10.1016/j.rse.2011.11.019, 2012.

Twardowski, M. S., Boss, E., Macdonald, J. B., Pegau, W. S., Barnard, A. H., and Zaneveld, J. R. V.: A model for estimating bulk refractive index from the optical backscattering ratio and the implications for understanding particle composition in case I and case II waters, Journal of Geophysical Research: Oceans, 106, 14129-14142, 10.1029/2000JC000404, 2001.

Valente, A., Sathyendranath, S., Brotas, V., Groom, S., Grant, M., Jackson, T., Chuprin, A., Taberner, M., Airs, R., Antoine, D., Arnone, R., Balch, W. M., Barker, K., Barlow, R., Bélanger, S., Berthon, J. F., Beşiktepe, Ş., Borsheim, Y., Bracher, A., Brando, V., Brewin, R. J. W., Canuti, E., Chavez, F. P., Cianca, A., Claustre, H., Clementson, L., Crout, R., Ferreira, A., Freeman, S., Frouin, R., García-Soto, C., Gibb, S. W., Goericke, R., Gould, R., Guillocheau, N., Hooker, S. B., Hu, C., Kahru, M., Kampel, M., Klein, H., Kratzer, S., Kudela, R., Ledesma, J., Lohrenz, S., Loisel, H., Mannino, A., Martinez-Vicente, V., Matrai, P., McKee, D., Mitchell, B. G., Moisan, T., Montes, E., Muller-Karger, F., Neeley, A., Novak, M., O'Dowd, L., Ondrusek, M., Platt, T., Poulton, A. J., Repecaud, M., Röttgers, R., Schroeder, T., Smyth, T., Smythe-Wright, D., Sosik, H. M., Thomas, C., Thomas, R., Tilstone, G., Tracana, A., Twardowski, M., Vellucci, V., Voss, K., Werdell, J., Wernand, M., Wojtasiewicz, B., Wright, S., and Zibordi, G.: A compilation of global bio-optical in situ data for ocean colour satellite applications – version three, Earth Syst. Sci. Data, 14, 5737-5770, 10.5194/essd-14-5737-2022, 2022.

Vandermeulen, R. A., Mannino, A., Craig, S. E., and Werdell, P. J.: 150 shades of green: Using the full spectrum of remote sensing reflectance to elucidate color shifts in the ocean, Remote Sensing of Environment, 247, 111900, https://doi.org/10.1016/j.rse.2020.111900, 2020.

Werdell, P. J., and Bailey, S. W.: An improved in-situ bio-optical data set for ocean color algorithm development and satellite data product validation, Remote Sensing of Environment, 98, 122-140, https://doi.org/10.1016/j.rse.2005.07.001, 2005.

Whitmire, A. L., Pegau, W. S., Karp-Boss, L., Boss, E., and Cowles, T. J.: Spectral backscattering properties of marine phytoplankton cultures, Opt. Express, 18, 15073-15093, 10.1364/OE.18.015073, 2010.

Wiegmann, S., Liu, Y., and Bracher, A.: Absorption coefficient spectra (median) of non-algal particles during POLARSTERN cruise PS93.2. In: In supplement to: Liu, Yangyang; Boss, Emmanuel; Chase, Alison P; Xi, Hongyan; Zhang, Xiaodong; Röttgers, Rüdiger; Pan, Yanqun; Bracher, Astrid (2019): Retrieval of phytoplankton pigments from underway spectrophotometry in the Fram Strait. Remote Sensing, 11(3), 318, https://doi.org/10.3390/rs11030318, PANGAEA, 2019.

Zhang, X., and Hu, L.: Light Scattering by Pure Water and Seawater: Recent Development, Journal of Remote Sensing, 2021, doi:10.34133/2021/9753625, 2021.

Zibordi, G., and Berthon, J. F.: Coastal Atmosphere and Sea Time Series (CoASTS) and Bio-Optical mapping of Marine Properties (BiOMaP): the CoASTS-BiOMaP dataset, Earth Syst. Sci. Data, 16, 5477-5502, 10.5194/essd-16-5477-2024, 2024.